Understanding the surrounding effects on Raman optical activity signatures of a chiral cage system: Cryptophane-PP-111

Lou C.G. D'haese, Nicolas Daugey, Delphine Pitrat, Thierry Brotin, Josef Kapitán, Vincent Liégeois

Understanding the surrounding effects on Raman optical activity signatures of a chiral cage system: Cryptophane–PP–111

Lou C. G. D'haese[a], Nicolas Daugey[b], Delphine Pitrat[c], Thierry Brotin[c], Josef Kapitán[d], and Vincent Liégeois[a]

[a]Theoretical Chemistry Laboratory (LCT), Namur Institute of Structured Matter (NISM), University of Namur, 5000 Namur, Belgium
[b]Groupe Spectroscopie Moléculaire (GSM), Institut des Sciences Moléculaires (ISM), UMR–5255 CNRS, University of Bordeaux, 33405 Talence, France
[c]Laboratoire de Chimie de l'ENSL, UMR–5182 CNRS, University of Lyon, 69364 Lyon, France
[d]Department of Optics, Palacký University of Olomouc, 77146 Olomouc, Czech Republic

September 18, 2023

Abstract

Cryptophane molecules are cage-like structures consisting in two hemispheres, each made of three benzene rings. These hemispheres are bound together with three $-O(CH_2)_nO-$ linkers of various lengths giving rise to a plethora of cryptophane derivatives. Moreover, they are able to encapsulate neutral guests: CH_2Cl_2, $CHCl_3$, ...; and charged species: Cs^+, Tl^+, ... Finally, they exhibit chiroptical properties thanks to the *anti* arrangement of the linkers between the hemispheres.

This work focuses on the Raman optical activity (ROA) signatures of Cryptophane–111 ($n = 1$ for each linker). More specifically, we aim at simulating accurately its ROA spectra with and without a xenon atom inside its cavity. Experimental data (T. Buffeteau, *et al.*, *Phys. Chem. Chem. Phys.* **19**, 18303–18310 (2017)) have already demonstrated the effect of the encapsulation in the low-wavenumbers region. To generate the initial structures, we rely on the novel Conformer–Rotamer Ensemble Sampling Tool (CREST) program, developed by S. Grimme and co–workers. This is required due to the flexibility provided by the linkers. The CREST algorithm seems promising and has already been used to sample the potential energy surface (PES) of target systems before the simulation of their vibrational spectroscopies (K.D.R. Eikås, M.T.P. Beerepoot, K. Ruud, *J. Phys. Chem. A* **126**, 5458—5471 (2022)).

We observe large similarities between the two sets of conformers (one with and one without Xe encapuslated), demonstrating the robustness of the CREST algorithm. For corresponding structures, the presence of xenon pushed the two hemispheres slightly further apart. After optimization at the DFT level, only one unique conformer has a Boltzmann population ratio greater than 1 %, pointing out the relative rigidity of the cage. Based on this unique conformer, our simulations are in good agreement with the experimental data. Regarding xenon encapsulation, the (experimental and theoretical) ROA signatures at low wavenumbers are impacted: slight shifts in wavenumbers are observed as well as a decrease in relative ROA intensity for bands around $150\,cm^{-1}$. The wavenumber shifts were very well reproduced by our simulations, but the experimental decrease in the ROA intensity was unfortunately not reproduced.

1 INTRODUCTION

The first cryptophane derivative has been synthesized in the 1980s by A. Collet and co–workers in order to assign experimentally the absolute configuration and maximum optical rotation of CHFClBr, one of the smallest chiral molecules [1, 2]. Generally speaking, cryptophanes are polyaromatic systems consisting of two hemispheres, each made of three benzene rings connected together in *ortho* by three methylene groups (Figure 1). The two hemispheres are bound together with three $-O(CH_2)_nO-$ linkers, creating a lipophilic inner–cavity. Since the synthesis of the so–called **Cryptophane–A**, a plethora of cryptophanes, decorated with different substituents and having different linker lengths, has been synthesized [3–10].

Their ability to encapsulate a large range of atoms and molecules, neutral or charged, aroused people interest and contributed significantly to the development of these host cage–systems. They are able to encapsulate neutral guests, such as $CH_2Cl_2/CHCl_3$ [11] or methyloxirane [12–14], and charged species, such as Cs^+/Tl^+ [15–19], in organic solutions as in aqueous ones. In addition, xenon is another guest of high interest that can enter the cavity of small cryptophanes. The potential of these xenon–cryptophane complexes, as biological sensors, has been reported by several authors [20–23].

Besides, the cryptophane derivatives have two chiral forms (***PP*** and ***MM*** enantiomers) thanks to the *anti* arrangement of the linkers between the hemispheres. If we look on top of each hemisphere, ***PP*** means that the oxygen atoms of the linkers point to the right on the benzene rings. ***MM*** means that they point to the left. Furthermore, we can have the ***PM*** and ***MP*** forms, corresponding to the *syn* arrangement, which are achiral (Supporting Information, Figure S1). They are the two equivalent structures of the *meso* diastereoisomers. However, they can be made chiral by functionalizing only one of the two hemispheres. This functionalization, often by **−OMe** or **−OAc** groups, is also used to make cryptophanes water–soluble. To distinguish the different cryptophane derivatives, we use the following nomenclature: **Cr–[*PP*/*MM*]–KLM–X{Y}**. **Cr** means **Cryptophane**. The letters **K**, **L**, and **M** each refer to the number of $-CH_2-$ group for each linker. The letter **X** represents the grafted groups. Finally, the **{Y}** indicates the encapsulation of the **Y** guest (Figure 1). Using this nomenclature, **Cryptophane–A** can be rewritten **Cr–*PP*–222–$(OMe)_6$**.

Since cryptophane derivatives are chiral, they exhibit chiroptical properties. Among them, we are particularly interested in their Raman optical activity (ROA) signatures. This chiroptical techniques is based on the difference in the intensity of Raman scattering between circularly polarized radiations, left–handed and right–handed ones. The enantiomers generate spectra with opposite signs, allowing their distinction by the measurements of their ROA spectra. The ROA signatures are also sensitive towards the molecular environment. For cryptophanes, their host–guest interactions have been highlighted by ROA experimental measurements [24].

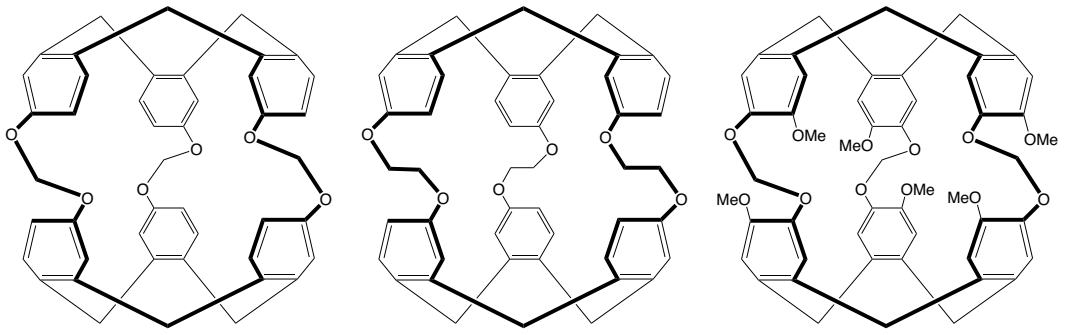

Figure 1: Sketches of different cryptophane derivatives: **Cr–*PP*–111** (left), **Cr–*PP*–222** (middle) and **Cr–*PP*–111–$(OMe)_6$** (right).

ROA spectroscopy, the optical activity counterpart of Raman spectroscopy, was predicted by L. D. Barron and A. D. Buckingham in 1971 [25]. It led to the first successful ROA measurements in 1972 [26–28]. In 1975, this phenomenom was confirmed by W. Hug [29]. During the late 1970s, the instruments have been significantly improved in order to facilitate the measurements of ROA spectra. The most important instrumental development of this technique was made by W. Hug in the late 1990s [30, 31], which led to the commercialization of the first ROA spectrometer in 2003 by BioTools.

Meanwhile, the theoretical methods to simulate ROA spectroscopy have been developed. The equations were known since 1971 [25] but the first full *ab initio* simulations were reported only in 1990 [32, 33]. The ROA spectra were computed at the Hartree–Fock (HF) level using a numerical differentiation approach for the evaluation of the Cartesian derivatives of the static polarizability tensors. Conventional basis sets have been used, implying an origin dependence for one of the different polarizability tensors. The approach was updated by using Gauge–including atomic orbitals (GIAOs) [34, 35] to remove this dependence. Moreover, the calculations, originally done at the static–limit, have been upgraded by considering the frequency of the laser beam thanks to time–dependent (TD) methodologies [36]. Following these developments, K. Ruud *et al.* reported the first simulation at the Density Functional Theory (DFT) level [37]. All these calculations were performed using numerical differentiations and the first fully consistent analytic implementation has been done in our laboratory by V. Liégeois *et al.*, at the HF level, in 2007 [38]. This implementation was based on the earlier works of O. Quinet and B. Champagne [39, 40]. Henceforth, the simulation of ROA spectra have become computational routines and implemented in different programs: Gaussian [41]; Turbomole [42]; and Dalton [43, 44], using the quasi–energy formulation of the response theory.

Recently, for ROA spectroscopy simulations, two main challenges have been pointed out: "the study of flexible systems where the analysis of their potential energy surface (PES) is the first obstacle to overcome" [45]; and "the description of weak intermolecular interactions and solvent effects" [46]. Our aim is precisely to simulate realistic ROA spectra of cryptophane derivatives and to take into account the solvent effects and the encapsulation of guest molecules. In this way, we decided to focus on **Cr–111**, that possesses a small inner–cavity and remarkable binding properties towards xenon [47]. Interestingly, a solvent like CH_2Cl_2 cannot enter its cavity and does not compete with xenon in solution. While this system seems quite rigid, it is still worth investigating its flexibility arising from the linkers between the hemispheres. Thus, our methodology begins with a sampling of the PES. Previously, only molecular mechanics programs have sampled the PES of cryptophane derivatives to assign their absolute configuration via DFT simulations of chiroptical spectroscopies [24, 48–52]. However, for this purpose, it has been demonstrated that the novel Conformer–Rotamer Ensemble Sampling Tool (CREST) program, developed by S. Grimme and co–workers, is suitable [53, 54]. Since it uses density functional tight–binding (DFTB) method, it is expected to be better than other conformational search programs. Moreover, this tool has already been used in recent articles to sample the PES of target systems before the simulation of their vibrational spectroscopies [55–57] and it seems very promising. Thus, we tested the performance of CREST on our organic cage–systems. For the solvent effects, we studied CH_2Cl_2, $CHCl_3$, and CCl_4 since they are greatly used as solvents to dissolve organic compounds. For the guest encapsulation, we have obviously chosen Xe for its high affinity with cryptophanes. This work will pave the way for the investigation of larger and more flexible cryptophane derivatives.

Our work is organized in different parts: i) the description of our methodology for the simulation of ROA spectra; ii) the analysis and comparison of the conformers generated by CREST and re–optimized at the DFT level for **Cr–111** and **Cr–111{Xe}** systems; iii) the influence of the solvent effects, described with different models, on the relative energies of the conformers; iv) the impact of xenon encapsulation and solvent effects on the vibrational normal

modes and ROA signatures; v) the comparison with experimental data; vi) the conclusions of our research.

2 COMPUTATIONAL DETAILS

As said above, the simulation of ROA spectra for flexible systems remains challenging. Thus, we have constructed a computational protocol to simulate their ROA spectra. The protocol is divided into 4 steps and depicted in Figure 2.

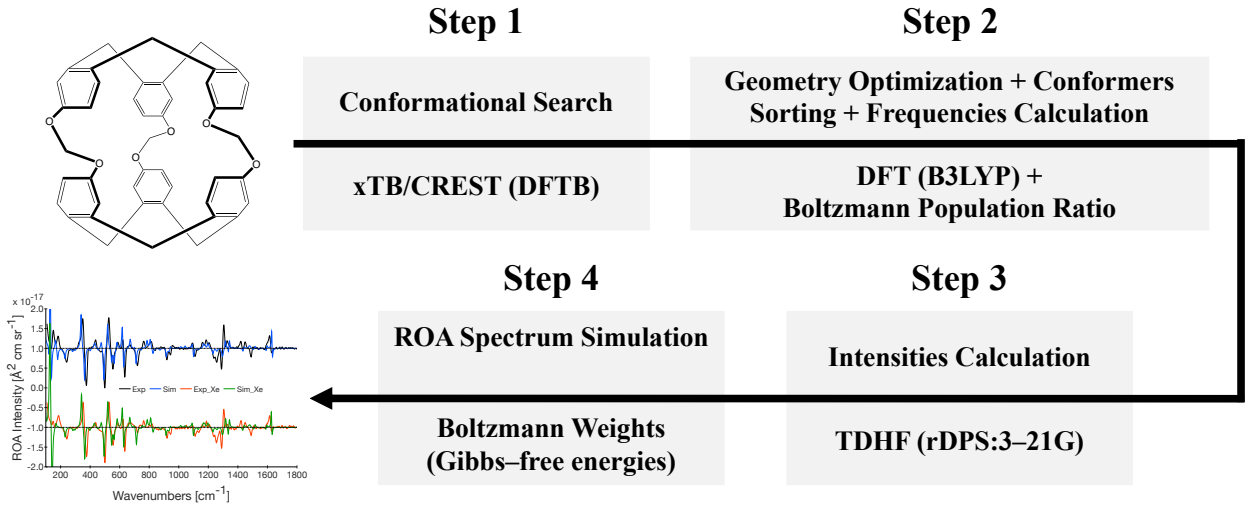

Figure 2: ROA spectra simulation protocol presented in this work.

First, the conformational search is performed on our system using CREST program and DFTB method (Section 2.1). Second, the different conformers obtained in step 1 are re–optimized at the DFT level. Then, the vibrational normal modes are calculated only for the conformers having a population ratio greater than 1 % (Section 2.2). Third, the Cartesian derivatives of the molecular properties responsible of the ROA intensity are evaluated (Section 2.3). Finally, the ROA spectrum is generated by a linear combination of the individual ROA spectra of the conformers. This linear combination takes into account the Boltzmann weights of the conformers, each based on their Gibbs–free energy (Section 2.4).

The 2$^{\text{nd}}$ and 3$^{\text{rd}}$ steps have been performed using Gaussian package [58]. The ROA spectra have been simulated and analyzed using DrawSuite programs [59], same for the visualization of the molecular structures and the vibrational normal modes.

2.1 Step 1 – Conformational Search

The CREST procedure to sample the PES is very meticulous [53, 54]. The conformational search uses the iMDT–GC algorithm which is based on the combination of root–mean–square deviations (RMSD) meta–dynamics (MTD) simulations and GFNx–xTB [60] calculations. A history–dependent biasing potential (Equation (1)) is applied to drive the structure away from the previous geometries:

$$V_{\text{bias}} = \sum_{i}^{n} k_i \, e^{-\alpha \Delta_i^2} \tag{1}$$

where n is the number of reference structures, k is the pushing strength, α determines the shape of the potential, and Δ is the RMSD value.

We used the GFN2–xTB [61] level of theory for the calculations. GFN2–xTB is a density functional tight–binding method, more precisely "DFTB3", with a modified D4 dispersion model [62] to calculate the dispersion energy.

The CREST procedure is divided into different steps:

1. At the beginning, the geometry optimization of the input structure and the calculation of its energy (called E_{input}) are done;
2. Then, 12 MTD simulations are performed using different settings (k and α) for the biasing contribution; each system has its own optimal settings and using a variety of parameters ensures the algorithm to perform well for all kind of systems;
3. Afterwards, several short molecular dynamics (MD) are performed on the 6 most stable conformers, at larger temperatures;
4. Finally, the genetic Z–matrix crossing (GC) procedure [63–65] is performed.

Each step generates conformations which are optimized in a multi–step filtering procedure with different threshold settings and energy windows. Next, these structures are saved in a Conformer–Rotamer Ensemble (CRE). CRE is a set of different conformers and their rotamers within a certain energy window around the same global potential energy minimum.

The algorithm is iterative. If one of the conformations has an energy value inferior to E_{input}, the entire procedure is restarted with this new structure as input.

We have changed some parameters to sample the PES of our system. We set the temperature to 300.00 K. We set the time step to 1.0 fs and the energy window to 20.00 kcal/mol, instead of 6.00 kcal/mol. With these parameters, we are sure to generate a sufficient number of conformers, which are going to be sorted after DFT optimizations.

2.2 Step 2 – Geometry Optimization with Conformers Sorting, followed by Frequencies Calculation

For small chiral systems, such as methyloxirane, heavy computational methods can be used to calculate the molecular properties of the system. However, our system is quite large and contains 87 atoms. Thus, we used a less cpu–time consuming method such as DFT. For the simulation of ROA spectroscopy, it has been demonstrated [41, 66, 67] that the exchange–correlation (XC) functional B3LYP [68, 69] performs well with a sufficiently complete basis set such as 6–31G*.

All the conformers are re–optimized at the DFT level. Rotamers and duplicates are removed thanks to an homemade code using similar criteria than CREST: energies, rotational constants, and RMSD values. Subsequently, the population ratios are calculated for each unique conformer, with respect to the most stable one, using the Boltzmann distribution. For the conformers having a population ratio greater than 1.0 %, corresponding to an electronic energy difference smaller than 2.75 kcal/mol, we calculated their vibrational normal modes at the DFT level.

2.3 Step 3 – Intensities Calculation

The evaluation of the ROA intensity needs the calculation of Cartesian derivatives of three polarizability tensors:

- α: electric dipole — electric dipole polarizability tensor;
- G': electric dipole — magnetic dipole polarizability tensor;
- A: electric dipole — electric quadrupole polarizability tensor.

The basis set needs diffuse functions to properly evaluate the polarizability tensors. However, these ones are not necessary for the geometry optimization and the vibrational normal modes calculation. Moreover, in 2004, G. Zuber and W. Hug introduced a new small basis set, rDPS:3–21G [70], with additional diffuse functions on the hydrogen atoms, specifically to evaluate the Cartesian derivatives of the polarizability tensors for the calculation of ROA intensity. This small basis set performs as good as aug–cc–pVDZ basis set, with a significant time saving.

Thus, for the conformers having a population ratio greater than 1.0 %, their Cartesian derivatives of the polarizability tensors are calculated at the TDHF/rDPS:3–21G level.

2.4 Step 4 – ROA Spectrum Simulation

At the double harmonic approximation, the ROA intensity associated to the p^{th} vibrational normal mode reads:

$$\mathrm{I}_{\mathrm{ROA},p} = \frac{1}{90}\left(\frac{\mu_0}{4\pi}\right)^2(\omega_0-\omega_p)^3\omega_0\frac{\hbar}{2\omega_p}\frac{1}{c}[\mathrm{A}\cdot a\mathrm{G}'_p + \mathrm{B}\cdot\beta^2_{Gp} + \mathrm{C}\cdot\beta^2_{Ap}]\mathrm{d}\Omega \tag{2}$$

where c is the speed of light in vacuum, $\hbar$ is the Planck constant divided by 2π, μ_0 is the vacuum magnetic permeability, $\omega_0 = 2\pi c\bar{\nu}_0$ is the angular frequency of the laser beam (related to the wavenumber $\bar{\nu}_0$), and $\hbar\omega_p$ is the energy associated to the vibrational transition $|0\rangle \rightarrow |1_p\rangle$. $\mathrm{d}\Omega$ is the cross–section. A, B, and C are multiplicative factors, which respectively amount to 0, 48, and 16 for the backward–scattering geometry and scattered circular polarization (SCP) modulation scheme.

The ROA invariants (aG'_p, β^2_{Gp}, β^2_{Ap}) are given by [71–74]:

$$\mathrm{aG}'_p = \frac{1}{9}\sum_{\mu,\nu}^{x,y,z}\left(\frac{\partial\alpha_{\mu\mu}}{\partial Q_p}\right)_0\left(\frac{\partial G'_{\nu\nu}}{\partial Q_p}\right)_0 \tag{3}$$

$$\beta^2_{Gp} = \frac{1}{2}\sum_{\mu,\nu}^{x,y,z}\left[3\left(\frac{\partial\alpha_{\mu\nu}}{\partial Q_p}\right)_0\left(\frac{\partial G'_{\mu\nu}}{\partial Q_p}\right)_0 - \left(\frac{\partial\alpha_{\mu\mu}}{\partial Q_p}\right)_0\left(\frac{\partial G'_{\nu\nu}}{\partial Q_p}\right)_0\right] \tag{4}$$

$$\beta^2_{Ap} = \frac{\omega_0}{2}\sum_{\mu,\nu}^{x,y,z}\sum_{\lambda,\kappa}^{x,y,z}\left[3\left(\frac{\partial\alpha_{\mu\nu}}{\partial Q_p}\right)_0\left(\frac{\epsilon_{\mu\lambda\kappa}\partial A_{\lambda\kappa\nu}}{\partial Q_p}\right)_0\right] \tag{5}$$

The Cartesian derivatives of the three polarizability tensors (evaluated in the 3$^{\text{rd}}$ step) are transformed into derivatives along the vibrational normal mode coordinates (evaluated in the 2$^{\text{nd}}$ step) using:

$$\left(\frac{\partial P}{\partial Q_p}\right)_0 = \sum_{i\zeta}\left(\frac{\partial P}{\partial R_{i\zeta}}\right)_0 Q^{\mathrm{c}}_{i\zeta,p}$$

where P is one of the polarizability tensors. $Q^{\mathrm{c}}_{i\zeta,p} = (1/\sqrt{m_i})Q_{i\zeta,p}$ is the Cartesian atomic displacement along the ζ Cartesian direction of the i^{th} atom associated to the p^{th} vibrational normal mode and $Q_{i\zeta,p}$ is the component, along the ζ Cartesian direction of the i^{th} atom for the p^{th} eigenvectors, that diagonalizes the mass–weighted Hessian.

For the conformers having a population ratio greater than 1.0 %, their ROA spectrum is simulated at the DFT/6–31G*//TDHF/rDPS:3–21G level. The final ROA spectrum is a linear combination of the individual ROA spectra of the conformers which are Boltzmann–weighted by their respective Gibbs–free energy. The Boltzmann weights can also be estimated based on the comparison with the ROA experimental spectrum. A visible wavelength of 532 nm has been

used to simulate our ROA spectra. The Maxwell–Boltzmann ($1/[1 - e^{(-\hbar\omega_p/(k_b T))}]$) factor has been used to account for the T–dependence of the populations of the vibrational levels in the spectra ($T = 300\,K$).

2.5 Surrounding effects

In addition, we have to incorporate the surroundings effects in our methodology, namely the encapsulation of a guest and the solvent effects (Figure 3).

We have considered the xenon as our guest since the cryptophanes have demonstrated their ability to bind this atom, thus acting as biological sensors [20–23]. However, the addition of a Xe atom, which possesses 54 electrons, in our DFT calculations is not trivial. Its interactions with the other electrons of the system are going to substantially increase the time and resources of the calculations. In order to properly calculate these interactions and to accelerate our calculations, effective core potentials (ECPs) have been used. These ones allow us to only compute the interactions with the valence electrons of the xenon. Nevertheless, it is necessary to consider enough electrons in our calculations to make realistic simulations.

Different ECPs, with some basis sets, have been tested: **dhf** [75] and **def2** [75] which take 26 valence electrons into account; **CRENBL** [76] which takes 18 valence electrons into consideration; and the others, **CRENBS** [76], **LANL2DZ** [77], **SBKJC** [78], and **Stuttgart–RLC** [79], which consider only 8 valence electrons in the calculations. This benchmark has been done on specific systems, XeF_2 (linear structure), XeF_4 (square structure), and XeF_6 (octahedral structure). The XC functional ωB97X–D has been used and the calculations have been done in gas phase. The fluorine atoms have been described with the 6–311G* basis set. Of course, the efficiency has been evaluated by comparing structural parameters and wavenumber values to experimental data [80–84]. The results are showed in the Supporting Information, Tables S1–S3. We observe that the 8 valence electrons ECPs have the largest relative differences. The triple–ζ basis sets have the smallest deviations, meaning they are very appropriate to describe the xenon. As a conclusion, the best ECP/basis set is **dhf/aug–cc–pwCVTZ–PP**.

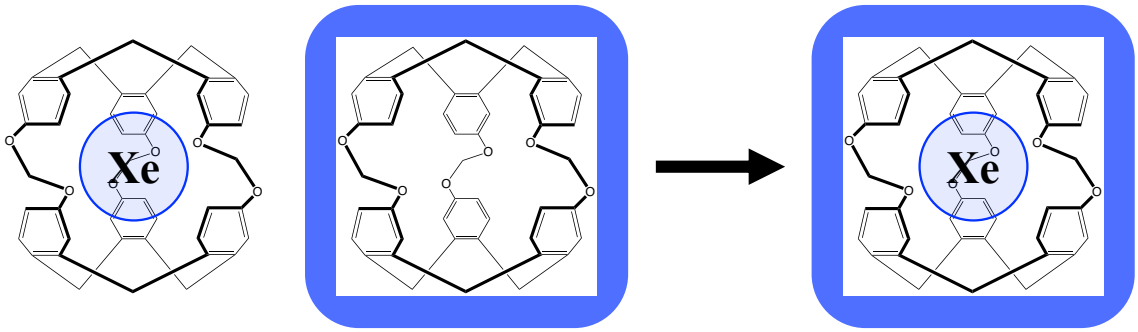

Figure 3: Representations of adding the surrounding effects to our system: xenon encapsulation (left), solvent effects (middle) and both (right).

For the solvent, we have considered chloromethane derivatives (namely CH_2Cl_2, $CHCl_3$, and CCl_4), which are greatly used in experimental measurements of the cryptophane derivatives. This kind of solvents mainly interacts with the solute through van der Waals forces so an implicit approach is usually sufficient. Moreover, the solvent effects are going to impact more strongly the relative electronic energies than the structures. Thus, the solvent is not included in the conformational search (1^{st} step). During both the geometry optimization/vibrational normal modes calculation at the DFT level (2^{nd} step) and the evaluation of the Cartesian derivatives of the polarizability tensors at the TDHF level (3^{rd} step), the solvent effects are accounted for implicitly using two approaches: the integral equation formalism of the polarizable continuum

model (IEF–PCM) [85] and the solvation model density (SMD) [86, 87]. The SMD approach is a special case of the IEF–PCM formalism where intrinsic Coulomb radii are used to describe the vdW surface of the cavity model instead of the vdW radii. This approach has been constructed to calculate more accurately the Gibbs–free energy of solvation ΔG^0_{sol}. Besides, the surface can be changed into the solvent excluded surface (SES) or the solvent accessible surface (SAS).

3 RESULTS AND DISCUSSION

First, we discussed the robustness of CREST program for generating the conformers of **Cr–111** and **Cr–111{Xe}** systems. Then, we investigated the impact of the solvent effects, described with different models, on the relative electronic energies. Next, we discussed the simulation of the ROA spectra of our cage–systems. There, we analyzed the impact of the xenon encapsulation and the solvent effects on the ROA signatures. Finally, we compared our results to experimental data in order to assess the efficiency of our protocol.

3.1 Conformational Search

The PES of our systems have been sampled using CREST program. For the **Cr–111** system, 20 conformers, numbered from **1** to **20**, have been generated in gas phase and ranked according to their GFN2–xTB energy, with respect to **1**. Then, the conformers have been re–optimized at the DFT level (B3LYP/6–31G*) in gas phase. Their relative electronic energy are showed in Table 1 (left). For the **Cr–111{Xe}** system, with a Xe atom inside the cavity, 19 conformers, numbered from **1{Xe}** to **19{Xe}**, have been generated in gas phase by CREST and ranked according to their GFN2–xTB energy, with respect to **1{Xe}**. Then, the conformers have been re–optimized at the DFT level (B3LYP/6–31G*) in gas phase. Their relative electronic energy, with respect to **1{Xe}**, are showed in Table 1 (right). The DFT results show that only **1** and **1{Xe}** participate to their final ROA spectrum, in gas phase.

Then, to highlight the differences and similarities of all these conformers, we have determined some structural measurements which are based on the position of the benzene ring centroids. These structural measurements are illustrated in Figure 4 and the values are reported in Table 2. For **Cr–111**, these parameters allow us to determine that **18** and **20** are rotamers. For **Cr–111{Xe}**, we determine that **13{Xe}/15{Xe}** are rotamers, **13{Xe}/16{Xe}** are duplicates like **14{Xe}/17{Xe}**. In Table 2, only one of these rotamers or duplicates is considered to simplify the comparison (so only **18**, **13{Xe}**, and **14{Xe}**). We have ordered the **Cr–111{Xe}** conformers based on their similarity with the **Cr–111** ones. As expected, the major impact of the xenon encapsulation on the structures is the increase of the distance a between the hemispheres by 0.1 to 0.4 Å.

From all these structures, only **1**, **2**, **1{Xe}**, and **2{Xe}** exhibit a "D3" symmetry, meaning that they have a principal C_3 axis and 3 secondary C_2 axes of rotation. The presence of the C_3 axis is indicated by a distance (b) equal to 0.00 Å between the hemispheres, an angle (ϕ) equal to 0.0° between the planes of the hemispheres, and three equal angles α, β, γ (Table 2). The structures of **1** and **2**, reported in Figure 5, are related with each other by rotations around each $-CH_2-$ linker group (similar observations are noticed for **1{Xe}** and **2{Xe}**). The orientation of the normal to the $-CH_2-$ plane, with respect to the C_3 axis, ranges from 32.9° (**1**) to −73.4° (**2**). These rotations induce the hemispheres of **2** to become closer than those of **1**, (from 5.19 Å to 4.28 Å, in Table 2). In addition, the alignment of the hemispheres of **2** is better than the one of **1** as pointed out by α, β, γ angles close to 60° for **2**.

Table 1: Relative electronic energies (in kcal/mol) of the different conformers of **Cr–111** (left) and **Cr–111{Xe}** (right), with respect to **1/1{Xe}**, optimized with GFN2–xTB and B3LYP in gas phase. Boltzmann population ratio, greater than 1 %, are reported in parentheses. Rotamers or duplicates are indicated by asterisks.

Numb.	GFN2–xTB	B3LYP	Numb.	GFN2–xTB	B3LYP
1	**0.00 (100%)**	**0.00 (100%)**	**1{Xe}**	**0.00 (100%)**	**0.00 (100%)**
2	**0.34 (56.9%)**	8.40	**2{Xe}**	**2.57 (1.3%)**	17.31
3	4.53	7.82	**3{Xe}**	6.55	14.39
4	5.17	7.18	**4{Xe}**	7.20	4.06
5	5.77	11.00	**5{Xe}**	7.79	12.61
6	6.82	4.11	**6{Xe}**	9.67	19.58
7	8.39	8.35	**7{Xe}**	10.94	12.83
8	9.12	9.33	**8{Xe}**	11.57	12.31
9	10.15	8.25	**9{Xe}**	11.58	12.06
10	10.34	8.32	**10{Xe}**	11.65	11.65
11	10.45	8.24	**11{Xe}**	12.02	13.50
12	12.15	6.56	**12{Xe}**	12.95	6.58
13	13.55	8.86	**13{Xe}**	14.27	7.56
14	13.74	9.48	**14{Xe}**	14.50	7.74
15	13.79	8.06	**15{Xe}**	14.99	7.56*
16	14.06	8.09	**16{Xe}**	15.11	7.56*
17	17.91	10.74	**17{Xe}**	15.73	7.74*
18	17.96	10.07	**18{Xe}**	18.68	9.36
19	18.23	10.79	**19{Xe}**	18.84	10.08
20	19.40	10.07*			

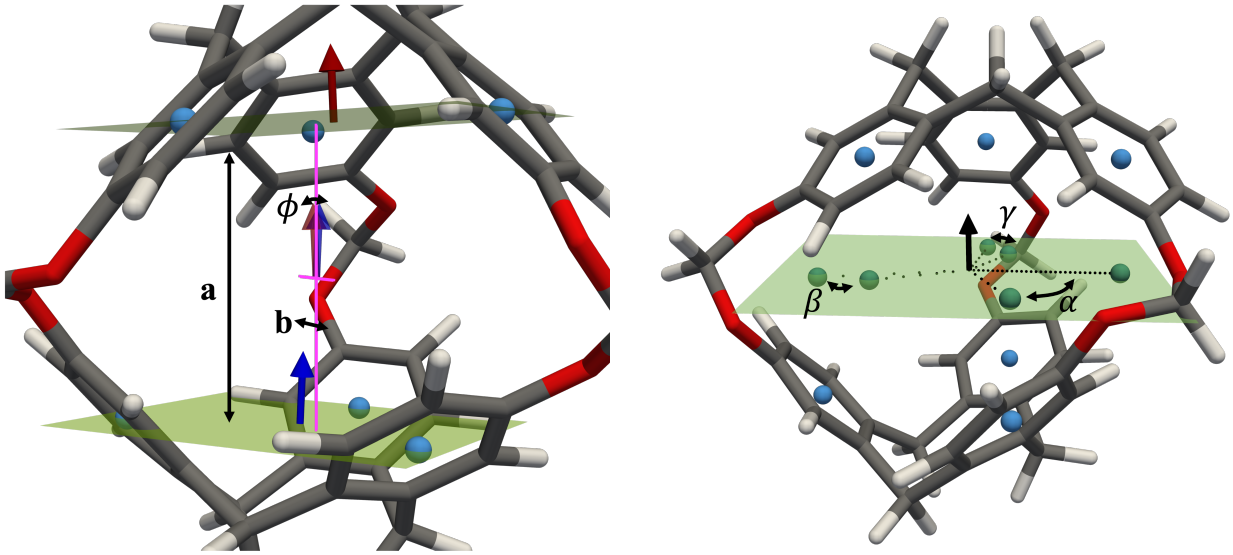

Figure 4: Illustration of the structural parameters, distances a and b (in Å) and angles ϕ, α, β, and γ (in °), on **4**. The centroids of the benzene rings are represented by blue spheres. (Left) The blue spheres of each hemisphere determine a plane, represented in light green, with their normal represented by red/blue arrows. (Right) The averaged plane is also represented in light green and its normal is represented by a black arrow. The projection of the blue spheres on this averaged plane are represented by green spheres.

Table 2: Structural parameters of the **Cr–111** and **Cr–111{Xe}** conformers. The distance a and b are in Å. The angles ϕ, α, β, and γ are in °.

Numb.	a	b	ϕ	α	β	γ	Numb.	a	b	ϕ	α	β	γ
1	5.19	0.00	0.0	19.3	19.3	19.3	**1{Xe}**	5.30	0.00	0.0	19.4	19.4	19.4
2	4.28	0.00	0.0	61.0	61.0	61.0	**2{Xe}**	4.57	0.00	0.0	61.7	61.7	61.7
3	4.45	0.42	4.4	42.8	60.8	61.3	**3{Xe}**	4.78	0.31	6.7	47.1	60.3	61.0
4	4.85	1.41	5.3	15.8	15.8	63.6	**5{Xe}**	5.15	1.06	2.8	19.1	19.1	59.8
5	4.61	1.11	4.9	16.8	61.7	61.7	**6{Xe}**	4.90	0.98	5.9	20.3	60.0	60.0
6	5.25	0.55	3.5	15.2	20.5	36.2	**4{Xe}**	5.39	0.43	4.2	16.8	20.9	34.3
7	4.84	1.34	7.7	13.0	37.1	64.7	**7{Xe}**	5.13	1.09	6.5	16.4	37.9	61.9
8	4.74	1.35	8.7	12.3	49.9	64.5	**11{Xe}**	5.15	0.89	6.5	19.3	35.5	59.7
9	4.73	0.90	7.8	35.4	35.4	64.0	**10{Xe}**	5.08	0.75	8.5	37.3	37.3	62.6
10	4.64	0.73	8.1	36.9	45.8	63.2	**9{Xe}**	5.03	0.59	8.1	39.2	40.2	61.0
11	4.60	0.64	8.5	44.6	44.6	63.3	**8{Xe}**	4.93	0.49	8.2	45.6	45.6	62.0
12	5.27	0.85	3.4	11.5	38.3	38.3	**12{Xe}**	5.42	0.72	3.8	13.7	37.0	37.0
13	5.09	1.21	0.2	9.5	40.5	53.3							
14	4.92	1.43	3.9	7.6	54.0	54.0							
15	5.28	0.59	3.2	16.1	34.1	38.7	**13{Xe}**	5.45	0.50	3.9	17.5	33.2	37.5
16	5.30	0.20	2.3	21.3	32.3	32.3	**14{Xe}**	5.46	0.18	3.2	21.7	32.5	32.5
17	4.87	0.73	5.6	31.0	49.3	52.2							
18	5.23	0.34	0.6	30.8	34.7	40.0	**18{Xe}**	5.44	0.31	0.5	31.1	34.7	39.4
19	4.97	0.00	0.0	38.6	38.6	38.6	**19{Xe}**	5.42	0.00	0.0	36.1	36.1	36.0

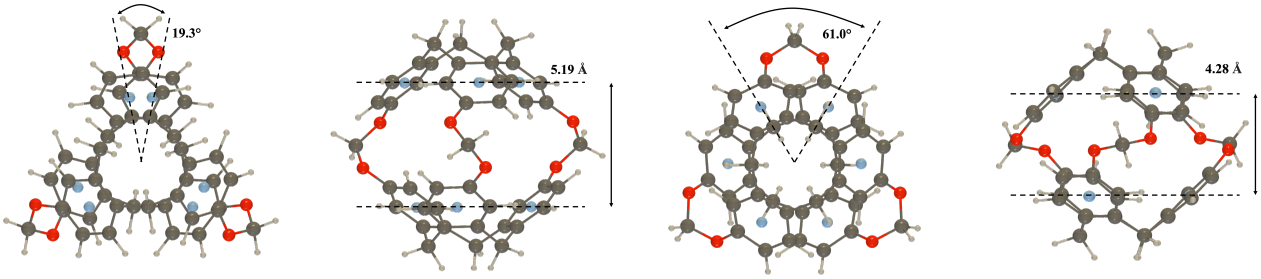

Top–view **1** Side–view **1** Top–view **2** Side–view **2**

Figure 5: Sketches of **1** and **2**, with the benzene rings centroids represented by light blue spheres.

3.2 Solvent effects on the conformers and their energies

3.2.1 Cr–111 system

We took the 20 conformers, **1** to **20**, generated by CREST and we re–optimized them in B3LYP/6–31G*, in CH_2Cl_2. The solvent effects have been computed implicitly with two models: IEF–PCM/vdW and SMD/vdW. We also used the SMD model with SAS. The relative electronic energies of the different conformers, with respect to **1**, are represented in Table 3.

The results point out that only **1** participates to the final ROA spectrum, regardless of the implicit model used to describe the solvent. Besides, we observe a stabilization or destabilization for the conformers going from gas phase to IEF–PCM/vdW and SMD/vdW (from **black cross** to **red square** and **blue triangle** in Figure 6). The impact is stronger for SMD/vdW than IEF–PCM/vdW. For the SMD/SAS model, the relative electronic energies are closer to the gas phase ones (**green circle** in Figure 6). Subsequently, we see that a hole is present inside the cavity for the vdW surface and the SES (the SES being the smoothed vdW surface) meaning

Table 3: Relative electronic energies (in kcal/mol), with respect to **1**, optimized with B3LYP in gas phase and CH_2Cl_2, with different implicit models. Boltzmann population ratio, greater than 1 %, are reported in parentheses. Rotamers or duplicates are indicated by asterisks.

Numbering	Gas phase	IEF–PCM/vdW	SMD/vdW	SMD/SAS
1	**0.00 (100%)**	**0.00 (100%)**	**0.00 (100%)**	**0.00 (100%)**
2	8.41	9.53	10.62	9.14
3	7.82	8.03	8.38	7.99
4	7.18	7.98	8.28	7.20
5	11.00	12.07	12.70	11.20
6	4.11	3.64	3.45	3.88
7	8.35	8.48	8.42	8.23
8	9.33	9.54	9.59	9.29
9	8.25	7.51	7.22	8.04
10	8.32	7.57	7.31	8.22
11	8.24	7.36	7.29	8.18
12	6.56	5.58	5.08	6.13
13	8.86	7.89	7.47	8.56
14	9.48	8.68	8.42	9.20
15	8.06	7.00	6.49	7.65
16	8.09	7.11	6.75	7.63
17	10.74	8.97	8.33	10.36
18	10.07	8.28	7.62	9.48
19	10.79	8.78	7.99	10.34
20	10.07*	8.28*	7.62*	9.48*

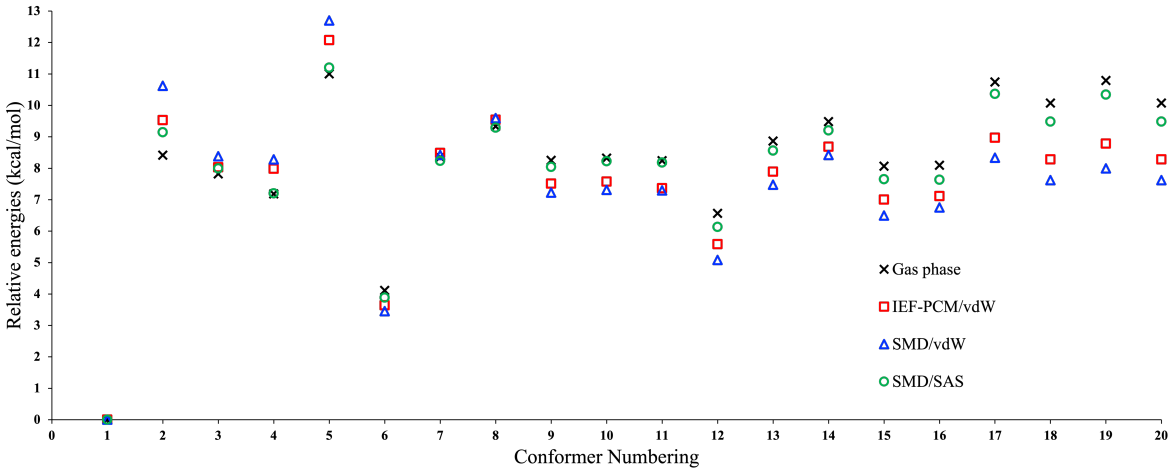

Figure 6: Relative electronic energies (in kcal/mol) of **Cr–111** conformers, with respect to **1**, optimized in B3LYP in gas phase and in CH_2Cl_2 with different implicit models.

that the solvent is considered in the cavity. However, it has been experimentally proved that the solvent is too big for entering in the cavity. Thus, the SAS model, where the surface is wider and completely covers the whole system, will be chosen.

In addition, we have also studied $CHCl_3$ and CCl_4, with the SMD/SAS model, since they are greatly used as organic solvents. Thus, the 20 conformers have been re–optimized in B3LYP/6–31G*, in $CHCl_3$ and CCl_4. Their relative electronic energy, with respect to **1**, are reported in Supporting Information, Table S4 and Figure S2. The results show that only **1**

participates to the final ROA spectrum, regardless of the solvent. Moreover, no significant or systematic impacts are observed on the relative electronic energies.

3.2.2 Cr–111{Xe} system

We took the 19 conformers, **1{Xe}** to **19{Xe}**, generated by CREST and we re–optimized them in B3LYP/6–31G*, in CH_2Cl_2. The solvent effects have been computed implicitly with two models: IEF–PCM/vdW and SMD/vdW. We also used the SMD model with SAS. The relative electronic energies of the different conformers, with respect to **1{Xe}**, are represented in Table 4. We notice that only **1{Xe}** participates to the final ROA spectrum, regardless of the implicit model used to describe the solvent.

Table 4: Relative electronic energies (in kcal/mol), with respect to **1{Xe}**, optimized with B3LYP in gas phase and CH_2Cl_2, with different implicit models. Boltzmann population ratio, greater than 1 %, are reported in parentheses. Rotamers or duplicates are indicated by asterisks.

Numbering	Gas phase	IEF–PCM/vdW	SMD/vdW	SMD/SAS
1{Xe}	**0.00 (100%)**	**0.00 (100%)**	**0.00 (100%)**	**0.00 (100%)**
2{Xe}	17.31	18.43	19.23	17.55
3{Xe}	14.39	14.67	14.91	14.26
4{Xe}	4.06	3.65	3.69	3.80
5{Xe}	12.61	13.37	13.70	12.36
6{Xe}	19.58	20.65	21.16	19.40
7{Xe}	12.83	12.93	13.08	12.45
8{Xe}	12.31	11.67	11.55	11.90
9{Xe}	12.06	11.49	11.34	11.68
10{Xe}	11.65	11.03	10.85	11.28
11{Xe}	13.50	13.76	13.81	13.05
12{Xe}	6.58	5.73	5.64	6.10
13{Xe}	7.56	6.63	6.43	7.12
14{Xe}	7.74	6.82	6.74	7.27
15{Xe}	7.56*	6.63*	6.43*	7.12*
16{Xe}	7.56*	6.63*	6.43*	7.12*
17{Xe}	7.74*	6.82*	6.74*	7.27*
18{Xe}	9.36	7.82	7.52	8.79
19{Xe}	10.08	8.42	7.94	9.61

3.3 Vibrational Normal modes and ROA Spectra

The conformers of **Cr–111** and **Cr–111{Xe}** have been successfully generated by CREST program. We have determined that only one unique conformer was participating to the final ROA spectrum for both molecules, in gas phase as well in solution, regardless of the implicit model or the solvent used. Therefore, no weightening of the individual spectra is necessary. For these systems (**1** and **1{Xe}**), the Cartesian derivatives of the three polarizability tensors have been evaluated at the TDHF/rDPS:3–21G level. Then, these quantities have been transformed into derivatives along the normal mode coordinates in order to compute their ROA spectrum (Equations (2) to (5)). Since enantiomers have opposite ROA spectra, only the ***PP*** enantiomer ROA spectrum has been simulated.

3.3.1 Surrounding Effects – Xenon Encapsulation

First, we decided to compare the global ROA spectra of **1** and **1{Xe}** (Supporting Information, Figure S3), in gas phase, to highlight the impact of xenon encapsulation. The global spectrum is slightly impacted by the xenon inside the cavity. Only the 50—300 cm^{-1} wavenumber range signatures are modified upon xenon encapsulation (see Figure 7).

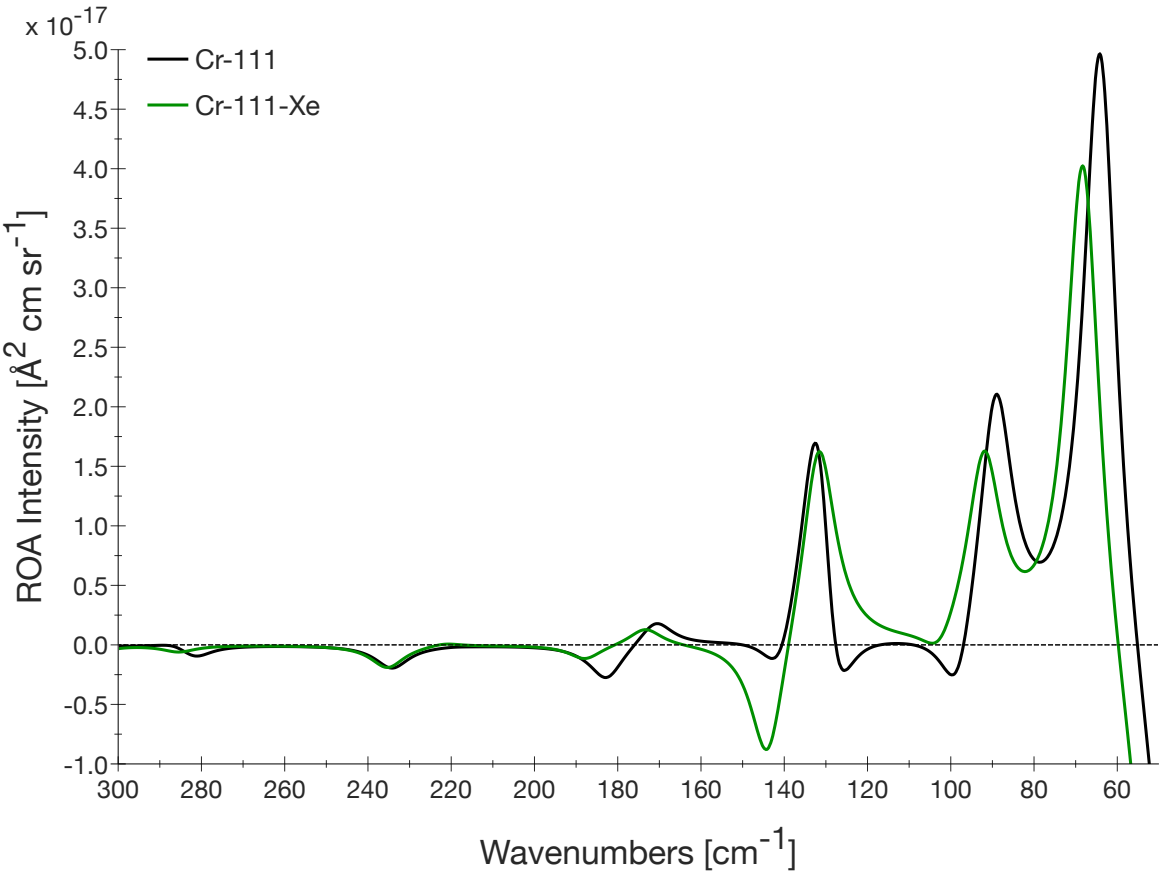

Figure 7: Simulated ROA backward–scattering spectra (at 532 nm) of **1**–***PP*** and **1**–***PP*{Xe}**, in gas phase, in the 50—300 cm^{-1} wavenumber range. The vibrational normal modes were evaluated at the B3LYP/6–31G* level, whereas the polarizabilities and their geometrical derivatives were evaluated at the TDHF/rDPS:3–21G level. Each transition is represented by a Lorentzian function with a FWHM of 10 cm^{-1} and no multiplicative factor is used to scale the vibrational frequencies.

When looking more particularly in the 120—150 cm^{-1} wavenumber range, we observe different impacts: the disappearance of the peak at 126 cm^{-1}, the slight decrease of the absolute intensity of the peak around 132 cm^{-1}, and the increase in the absolute intensity of the peak at 142 cm^{-1}. Besides, the peak at 132 cm^{-1} is slightly shifted to lower wavenumbers while the peaks around 65 cm^{-1} and 90 cm^{-1} are shifted to higher wavenumbers.

For the 120—150 cm^{-1} wavenumber range, we analyzed the vibrational normal modes and their ROA intensities. According to their "D3" symmetry group, **1** and **1{Xe}** have respectively 255 and 258 normal modes which are distributed into three irreducible representations (A1, A2, and doubly–degenerated E). So **1** has 43 modes A1, 42 modes A2, and 85 modes E and **1{Xe}** has 44 modes A1, 42 modes A2, and 86 modes E. In this region, where most changes are observed, we have the normal modes 10 to 15 for **1** and 13" to 18" for **1{Xe}** (Table 5). The normal modes 10–11, 14–15, 14"–15", and 17"–18" are doubly–degenerated, so E. The normal modes 12 and 13" are A1 while the normal modes 13 and 16" are A2. Their Cartesian displacements are represented using spheres (Figure 8). Only minor changes are observed upon xenon encapsulation.

Regarding their wavenumbers and ROA intensities (Table 5), upon xenon encapsulation, all the normal modes are shifted to higher wavenumbers. The normal modes 10–11 are especially hugely shifted with respect to the other ones. It leads to the disappearance of the peak at 126 cm^{-1}. The peak at 132 cm^{-1} becomes a superposition of three normal modes (13" to 15"), while only 12 contributes for **1**. The intensities of normal modes 12 and 13" are very similar. The total absolute intensities of normal modes 10–11 decreases upon xenon encapsulation by a factor of 4.0 (to become 14"–15") while the total absolute intensities of normal modes 14–15 increases by a factor of 2.35 (to become 17"–18"). The absolute ROA intensities of normal modes A2 (13 and 16") are largely inferior to the others and do not contribute to the ROA spectra.

Table 5: Wavenumber (in cm^{-1}) and ROA intensity (in $Å^2$/sr) values for the normal modes of **1–*PP*** (left) and **1–*PP*{Xe}** (right), in gas phase, in the 120–150 cm^{-1} wavenumber range. The vibrational normal modes were evaluated at the B3LYP/6–31G* level, whereas the polarizabilities and their geometrical derivatives were evaluated at the TDHF/rDPS:3–21G level.

Normal Modes	$\overline{\nu}$	Intensity	Normal Modes	$\overline{\nu}$	Intensity
10–11 (E)	128.15	-2.53 x 10^{-16}	14"–15" (E)	132.40	-6.36 x 10^{-17}
12 (A1)	131.80	4.40 x 10^{-16}	13" (A1)	131.90	3.33 x 10^{-16}
13 (A2)	136.90	6.47 x 10^{-20}	16" (A2)	137.60	3.68 x 10^{-19}
14–15 (E)	141.20	-7.18 x 10^{-17}	17"–18" (E)	143.95	-1.69 x 10^{-16}

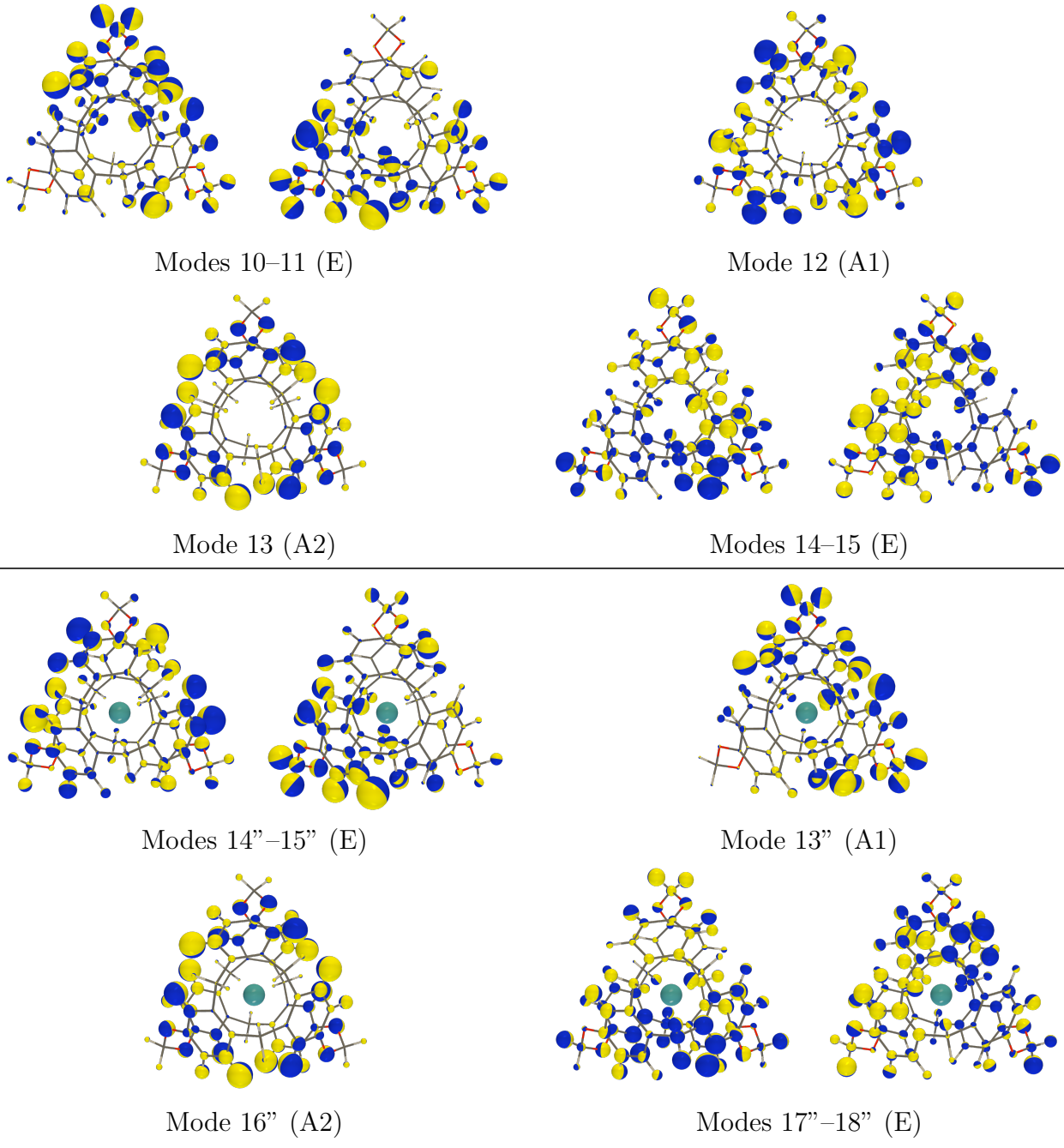

Figure 8: Sketch of the B3LYP/6–31G* (gas phase) vibrational normal modes of **1**–***PP*** (top) and **1**–***PP*****{Xe}** (bottom) in the 120–150 cm^{-1} wavenumber range. The direction of atomic displacements is perpendicular to the junction plane between the two hemispheres of distinct color, and its amplitude is proportional to the radius of the sphere.

3.3.2 Surrounding Effects – Solvent Effects

Second, we have studied the solvent effects on the ROA signatures. The global ROA spectra of **Cr–*PP*–111** obtained in gas phase and in CH_2Cl_2 (with IEF–PCM/vdW, SMD/vdW, and SMD/SAS models) are reported in Supporting Information, Figure S4. The global ROA spectrum is only slightly impacted by the solvent effects. Similarly to the xenon encapsulation, only the 50—300 cm^{-1} wavenumber range signatures are modified by the presence of the solvent (Figure 9). Contrary to the xenon encapsulation, the impact of the solvent effects is less significant. We notice only minor shifts that, at most, amount to 2 cm^{-1} in the 120—150 cm^{-1} wavenumber range (Table 6). Regarding the ROA intensities, the largest impact is observed for IEF–PCM/vdW solvent model with an increase in absolute intensity ranging from 30 % to 75 %. The ROA spectrum simulated with the SMD/SAS model is the most similar to the gas phase one with only a general slight shift to lower wavenumbers.

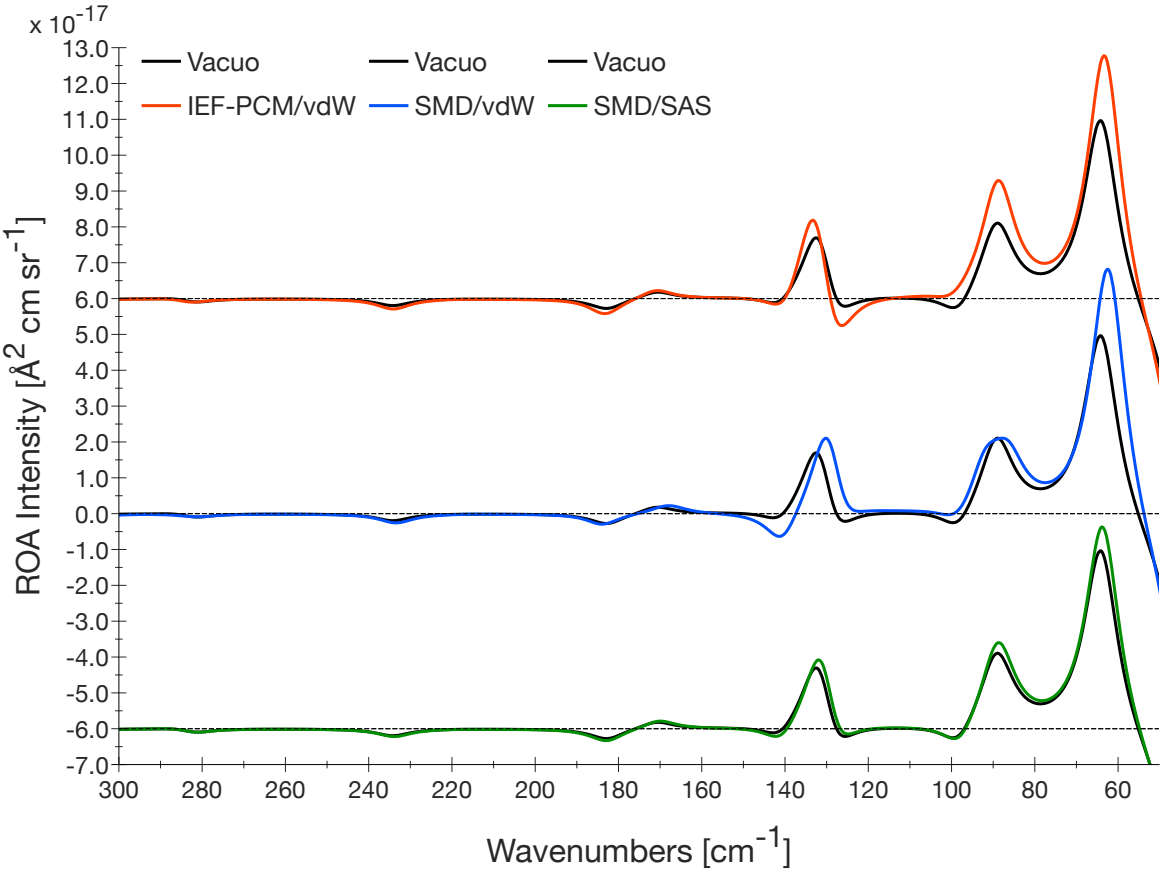

Figure 9: Simulated ROA backward–scattering spectra (at 532 nm) of **1**–***PP*** in gas phase and CH_2Cl_2 with different implicit models (IEF–PCM/vdW, SMD/vdW, and SMD/SAS), in the 50—300 cm^{-1} wavenumber range. The vibrational normal modes were evaluated at the B3LYP/6–31G* level, whereas the polarizabilities and their geometrical derivatives were evaluated at the TDHF/rDPS:3–21G level. Each transition is represented by a Lorentzian function with a FWHM of 10 cm^{-1} and no multiplicative factor is used to scale the vibrational frequencies.

In addition, we have also investigated $CHCl_3$ and CCl_4 with the SMD/SAS model. Their ROA spectra are reported in Supporting Information, Figures S5 and S6. We observe no significant impact from CH_2Cl_2 to $CHCl_3$ or CCl_4.

Table 6: Wavenumber (top, in cm^{-1}) and ROA intensity (bottom, in $Å^2$/sr) values for the normal modes of **1–*PP***, in gas phase and in CH_2Cl_2 with different implicit models, in the 120–150 cm^{-1} wavenumber range. The vibrational normal modes were evaluated at the B3LYP/6–31G* level, whereas the polarizabilities and their geometrical derivatives were evaluated at the TDHF/rDPS:3–21G level.

Normal Modes	Gas phase	IEF–PCM/vdW	SMD/vdW	SMD/SAS
10–11 (E)	128.15	128.15	126.40	127.85
12 (A1)	131.80	132.80	129.60	131.20
13 (A2)	136.90	136.60	138.20	136.30
14–15 (E)	141.20	140.15	140.70	140.90
Normal Modes	Gas phase	IEF–PCM/vdW	SMD/vdW	SMD/SAS
10–11 (E)	-2.53 x 10^{-16}	-3.63 x 10^{-16}	-2.45 x 10^{-16}	-2.87 x 10^{-16}
12 (A1)	4.40 x 10^{-16}	5.70 x 10^{-16}	5.21 x 10^{-16}	5.09 x 10^{-16}
13 (A2)	6.47 x 10^{-20}	-1.63 x 10^{-18}	-7.73 x 10^{-18}	-1.49 x 10^{-19}
14–15 (E)	-7.18 x 10^{-17}	-1.26 x 10^{-16}	-1.64 x 10^{-16}	-9.39 x 10^{-17}

3.4 Boltzmann Weights

Up to now, using XC functional B3LYP, only one conformer was taken into account in each system, **1** for **Cr–*PP*–111** and **1{Xe}** for **Cr–*PP*–111{Xe}**. Nevertheless, the evaluation of the relative energies might lack of explicit dispersion corrections [88]. Therefore, we have computed the Boltzmann population ratios (based on the relative Gibbs–free energies) using ωB97X–D and different Grimme's dispersion models (D2, D3, and D3BJ) on top of B3LYP for the conformers of **Cr–*PP*–111** (Table 7) and **Cr–*PP*–111{Xe}** (Supporting Information, Table S5). We observe that **2** becomes the most stable conformer while **1** has a population ratio of about 4—18 % when dispersion is included explicitly. Moreover, **3** becomes more stable than **1** with B3LYP–D3, B3LYP–D3BJ, and ωB97X–D. For **2{Xe}**, its relative Gibbs–free energy of 17.77 kcal/mol becomes only 4.71 kcal/mol with B3LYP–D3BJ and 7.72 kcal/mol with ωB97X–D. So, **1{Xe}** remains the most stable conformer.

However, it has been recently demonstrated that while the relative ordering of the conformers is impacted by the dispersion corrections, their vibrational optical activity signatures are less, or even not, affected by these corrections [56]. Moreover, the group of Kenneth Ruud has observed that the final Boltzmann–weighted B3LYP–D3 spectrum was in poorer agreement with respect to the experiment than the Boltzmann–weighted B3LYP one.

Based on these conclusions, we decide to keep B3LYP for the geometry optimization and the calculation of the vibrational normal modes. We also expect that the experimental ROA spectra will be mainly described by the ROA signatures of conformers **1**.

Table 7: Relative Gibbs–free energies (in kcal/mol) of the different conformers of **Cr–111**, with respect to **1**, optimized with different methods in gas phase. Boltzmann population ratio, greater than 1 %, are reported in parentheses. Rotamers or duplicates are indicated by asterisks.

Numb.	B3LYP	B3LYP–D2	B3LYP–D3	B3LYP–D3BJ	ωB97X–D
1	**0.00 (100%)**	**0.00 (4.3%)**	**0.00 (6.2%)**	**0.00 (6.6%)**	**0.00 (18.6%)**
2	7.98	**-1.87 (100%)**	**-1.66 (100%)**	**-1.62 (100%)**	**-1.00 (100%)**
3	6.49	**0.21 (3.1%)**	**-0.02 (6.4%)**	**-0.27 (10.4%)**	**-0.18 (25.2%)**
4	6.56	4.21	3.82	3.92	4.07
5	10.32	5.15	4.78	4.73	5.55
6	3.49	4.62	4.45	4.32	3.79
7	7.19	5.03	4.70	4.53	4.86
8	8.08	5.37	4.96	4.91	4.76
9	5.96	4.06	3.07	2.67	2.62
10	5.90	3.58	2.71	2.48	2.28
11	5.75	3.25	2.58	2.25	2.44
12	5.30	7.30	7.04	6.79	6.48
13	6.97	8.15	7.40	7.07	6.57
14	7.76	7.76	7.19	7.01	7.03
15	6.49	9.09	8.59	8.32	7.62
16	6.65	9.10	8.46	8.25	7.61
17	7.51	9.46	7.11	-0.27*	6.25
18	7.57	9.17	7.11*	6.64	6.25*
19	6.63	11.51	7.05	6.34	5.24
20	7.57*	10.66	8.62	8.17	7.73

3.5 Simulations versus Experiments

Finally, we are going to compare our theoretical results to two sets of experimental data. For the first set, the ROA spectra have been recorded by N. Daugey, in CD_2Cl_2 at room temperature, and published in the article of T. Buffeteau [24]. For the second set, the ROA spectra have been recorded by J. Kapitán in $CDCl_3$ in the extended spectral range down to $50\,cm^{-1}$ with a custom-built ROA instrument at Palacký University Olomouc [89]. The samples were measured in a rectangular fused silica cell, the temperature was stabilised at 293 K, and the scattered circular polarization (SCP) modulation scheme was used in backscattering geometry, with an excitation wavelength of 532 nm. The sample concentration was set to $100\,mg\,mL^{-1}$ and the acquisition time was 2-6 hours. The laser power measured at the sample position was set to 82 mW to avoid saturating the CCD detector and to recover the ROA signal also in the vicinity of the solvent bands. ROA intensities were calibrated using a tungsten-halogen calibration source (SpectralWiz). Experimental intensities are given as the number of detected electrons per excitation energy in a wavenumber interval (e^-cm/J). For the comparison with the simulations, the experimental units are converted into $Å^2\,cm\,sr^{-1}$ by taking into account the various experimental conditions: solid angle, laser power, ... For the simulations, we evaluated the vibrational normal modes at the B3LYP/6–31G* level, the polarizabilities and their geometrical derivatives at the TDHF/rDPS:3–21G level, and the solvent effects with the SMD/SAS model. The xenon is described with dhf/aug–cc–pwCVTZ–PP.

Three conformers have been considered for **Cr–*PP*–111**: **1**, **2**, and **3**. Compared to the first set of experimental ROA spectra (Figure 10), the agreement is better for conformer **1** than conformers **2** and **3**. For instance, around $500\,cm^{-1}$, the negative-positive peaks (from

lower to higher wavenumbers) observed experimentally are well reproduced by conformer **1** while conformers **2** and **3** show peaks of opposite signs. Another significant discrepancy in the signatures of conformers **2** and **3** is their negative peak around 1350 cm^{-1} that is not observed experimentally.

To quantify the agreement between our simulations and the experimental ROA spectrum for **Cr–*PP*–111**, we have evaluated their overlap in the 200—1800 cm^{-1} wavenumber range while varying the relative percentage of the three conformers (Supporting Information, Table S6). The overlap value decreases with the increase of the percentage of conformers **2** and/or **3**. Therefore, we estimate that their population in the sample is less than 10 % altogether.

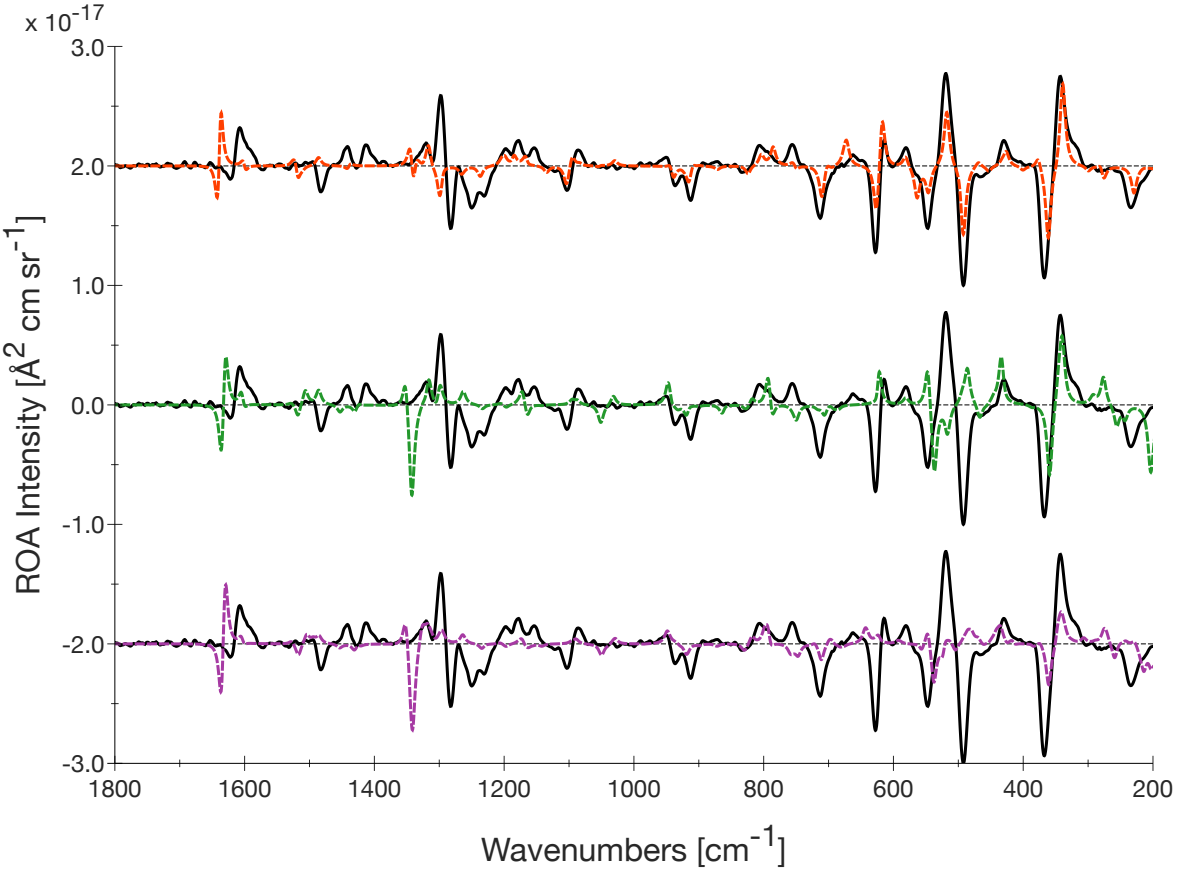

Figure 10: Experimental (**solid lines**, in **black**) and simulated (**dotted lines**, in **red** for **1**, in **green** for **2**, and in **purple** for **3**) backward–scattering ROA spectra (at 532 nm) of **Cr–*PP*–111**, in dichloromethane, in the 200—1800 cm^{-1} wavenumber range. In the simulated spectra, each transition is represented by a Lorentzian function with a FWHM of 10 cm^{-1}, and a multiplicative factor of **0.98** is used to scale the vibrational frequencies.

In conclusion, our simulations, based only on conformer **1**, are in good agreement with the experimental data, as indicated by the maximum overlap value (0.689) obtained. Thus, for the continuation of our investigation, only conformer **1** is considered for **Cr–*PP*–111**. The ROA spectra of **1** and **1{Xe}** are reported in Figure 11. A good agreement is also obtained for **1{Xe}** with respect to the experimental ROA spectrum. Moreover, similarly to our observations on the previous ROA spectra in gas phase, the experimental ones are only slightly impacted by the xenon encapsulation (in **black**, from top to bottom in Figure 11).

In their publication, T. Buffeteau *et al.* [24] have noticed that most changes, upon xenon encapsulation, appeared at low wavenumbers in their recorded ROA spectra (Figure 12, top). Especially, they highlighted a huge decrease in absolute intensity (around 80 %) of the peak at

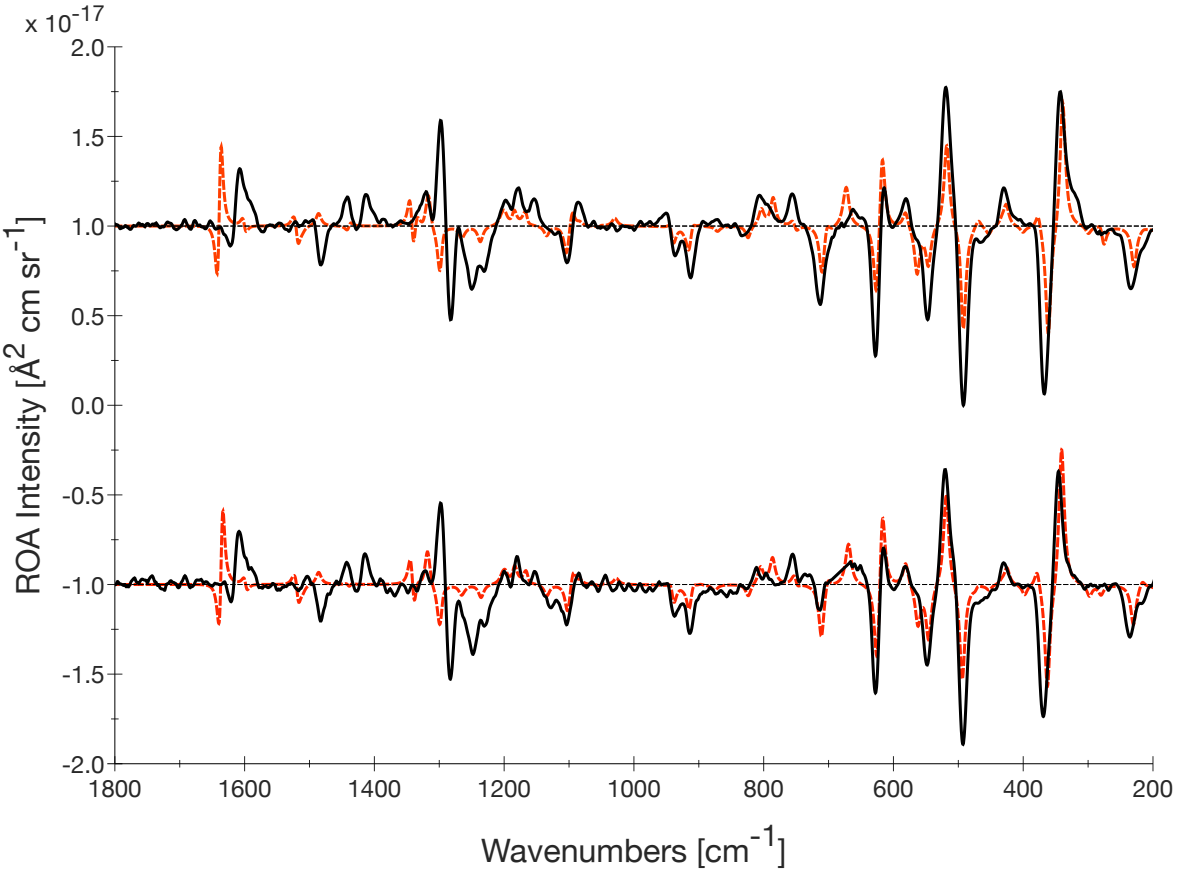

Figure 11: Experimental (**solid lines**, in **black**) and simulated (**dotted lines**, in **red**) backward–scattering ROA spectra (at 532 nm) of **Cr–*PP*–111** (top) and **Cr–*PP*–111{Xe}** (bottom), in dichloromethane, in the 200—1800 cm^{-1} wavenumber range. Only the conformers **1/1{Xe}** are considered. In the simulated spectra, each transition is represented by a Lorentzian function with a FWHM of 10 cm^{-1}, and a multiplicative factor of **0.98** is used to scale the vibrational frequencies.

143 cm^{-1} by the presence of xenon inside the cavity (top, from **black** to **blue**). They attributed this peak to a "breathing mode". We also note a slight shift towards lower wavenumbers of this peak. Below 150 cm^{-1}, a slight vertical offset is observed, probably due to corrections of the solvent artifacts. In our simulations (Figure 12, bottom), we observe a positive peak at around 150 cm^{-1} which is slightly shifted to lower wavenumbers (bottom, **black** to **blue**). However, contrary to the experimental data, the simulated peak intensity did not decrease when the xenon is encapsulated.

Finally, the second set of experimental data are compared to our simulations (Figure 13). Compared with the previous measurements, the two sets of experimental measurements are in very good agreement with each other. Below 150 cm^{-1}, these new ROA spectra highlight two positive peaks around 75 cm^{-1} and 95 cm^{-1}, which are reproduced by our simulations. However, these bands are less sensitive to the xenon encapsulation, especially in terms of relative intensity, than the signatures at 150 cm^{-1} but they exhibit significant shifts that are well reproduced in the simulations.

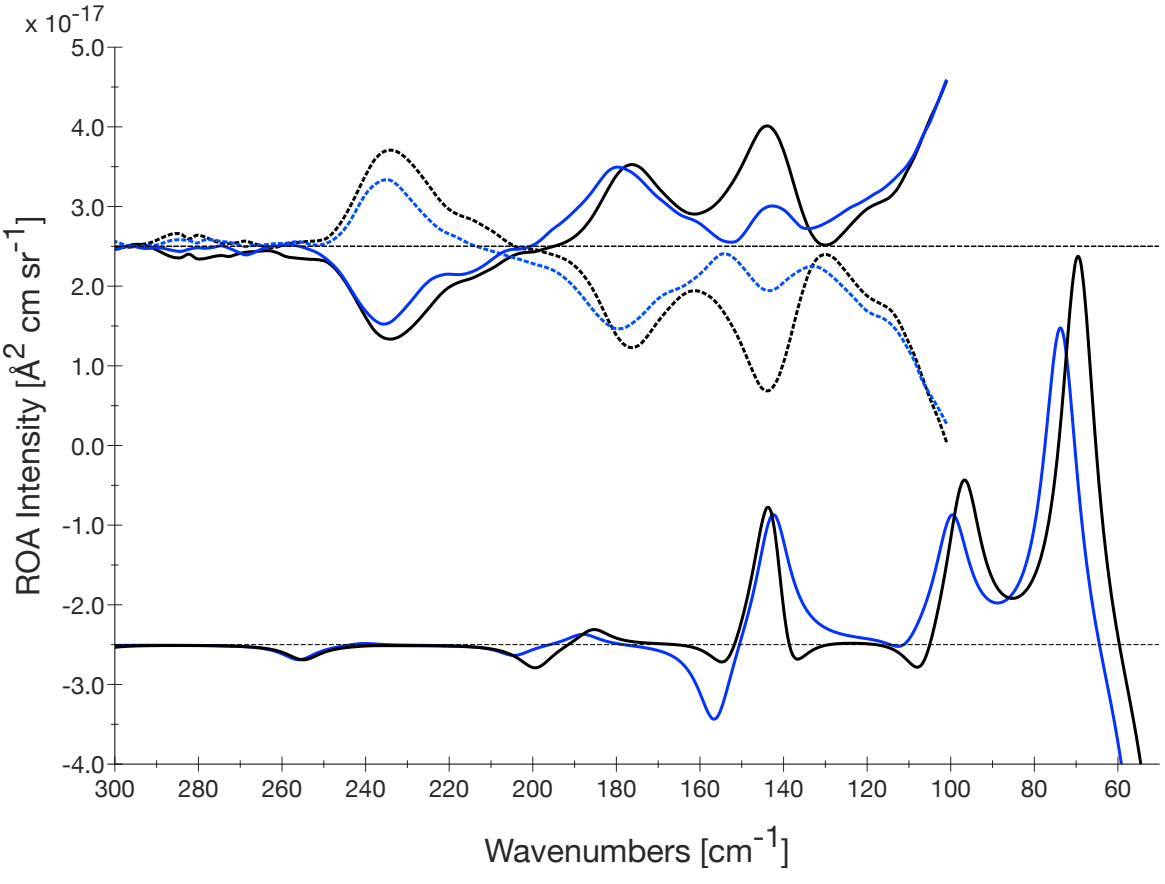

Figure 12: Experimental (top, [24]) and simulated (bottom) backward–scattering ROA spectra (at 532 nm) of **Cr–*PP*–111** (**black**) and **Cr–*PP*–111{Xe}** (**blue**), in dichloromethane, in the 50—300 cm^{-1} wavenumber range. The **dotted lines** are for the recorded **MM** enantiomers. In the simulated spectra, each transition is represented by a Lorentzian function with a FWHM of 10 cm^{-1}, and a multiplicative factor of **1.09** is used to scale the vibrational frequencies.

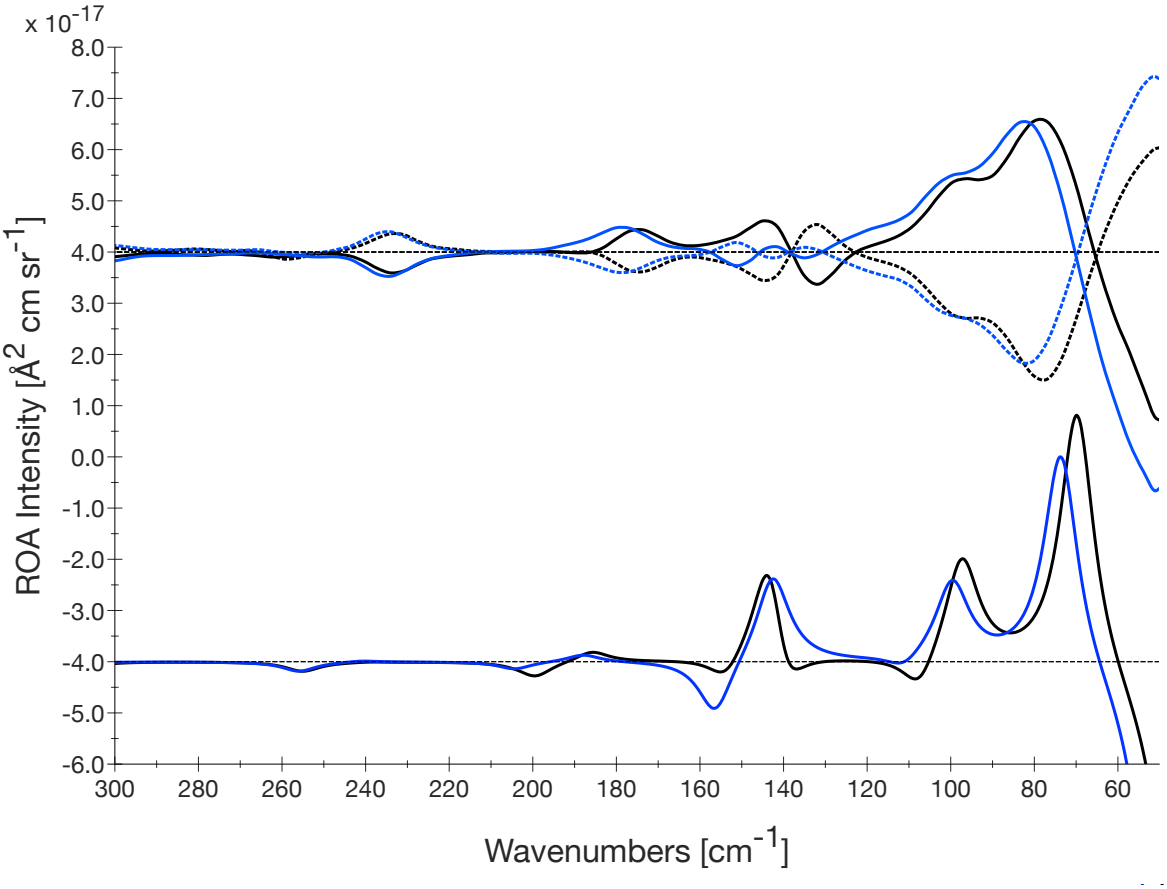

Figure 13: Experimental (top) and simulated (bottom) backward–scattering ROA spectra (at 532 nm) of **Cr–*PP*–111** (**black**) and **Cr–*PP*–111{Xe}** (**blue**), in chloroform, in the 50—300 cm^{-1} wavenumber range. The **dotted lines** are for the recorded **MM** enantiomers. In the simulated spectra, each transition is represented by a Lorentzian function with a FWHM of 10 cm^{-1}, and a multiplicative factor of **1.09** is used to scale the vibrational frequencies.

4 Conclusions

Using CREST program, we sampled the PES of **Cr–111** and **Cr–111{Xe}**. By analyzing their structural parameters, we observed huge similarities between the two sets of conformers, demonstrating the robustness of the CREST algorithm. For corresponding structures, the presence of xenon, inside the cavity, pushed the two hemispheres slightly further apart. After re–optimization at the DFT level, only one unique conformer had a population ratio greater than 1 %, pointing out the relative rigidity of the **Cr–111** cage.

Based on this unique conformer, our simulations were in good agreement with the two sets of experimental data. This contradicts the relative ordering of the conformers obtained with methods containing Grimme's dispersion model. Indeed, poorer agreement with respect to the experiment was observed with increasing relative population of **2** and/or **3**. The same conclusion has also been demonstrated by others [56, 90] for similar interconnected systems.

Regarding xenon encapsulation, the (experimental and theoretical) ROA signatures at low wavenumbers are impacted: slight shifts in wavenumbers have been observed as well as a decrease in absolute ROA intensity for bands around 150 cm^{-1}. The wavenumber shifts were very well reproduced by our simulations, but the experimental decrease in the ROA intensity was unfortunately not reproduced.

In conclusion, we have constructed a computational protocol to simulate ROA spectra for flexible systems, which uses the CREST program for generating conformers. For the solvent effects, we studied CH_2Cl_2, $CHCl_3$, and CCl_4 since they are greatly used as organic solvents. In our case, the impact was small, even smaller than the impact of the implicit model (IEF–PCM/vdW, SMD/vdW, SMD/SAS).

This work paves the way for the investigation of larger and more flexible cryptophane derivatives where an exponentially increasing number of conformers is expected. In the future, we will study other cryptophane derivatives with different guests such as **Cr–222** with CH_2Cl_2, $CHCl_3$, methyloxirane, Cs^+, Tl^+, ...

5 Acknowledgments

L.D. thanks the University of Namur (Belgium) for his FSR funding (Convention 1–9812–00). N.D., D.P., T.B. and V.L. acknowledge the French National Research Agency (ANR) for financial support of Project ANR CAORSS (ANR21–CE29–0006–01) and the Program Hubert Curien Tournesol AORTE n°46259SA for travel exchanges. J.K. acknowledges the financial support from the Grant Agency of the Czech Republic (22–04669S). V.L. thanks the F.R.S.–FNRS for his Research Associate position.

The calculations were performed on the computers of the Consortium des Équipements de Calcul Intensif (CÉCI) and particularly those of the Technological Platform of High–Performance Computing, for which we gratefully acknowledge the financial support of the University of Namur (Conventions Nos. U.G006.15, U.G018.19, U.G011.22, RW/1610468, and RW/GEQ2016).

6 References

[1] Canceill, J.; Lacombe, L.; Collet, A. Analytical optical resolution of bromochlorofluoromethane by enantioselective inclusion into a tailor-made cryptophane and determination of its maximum rotation. *J. Am. Chem. Soc.* **1985**, *107*, 6993–6996.

[2] Collet, A. Cyclotriveratrylenes and cryptophanes. *Tetrahedron* **1987**, *43*, 5725–5759.

[3] Garel, L.; Lozach, B.; Dutasta, J. P.; Collet, A. Remarkable effect of the receptor size in the binding of acetylcholine and related ammonium ions to water-soluble cryptophanes. *J. Am. Chem. Soc.* **1993**, *115*, 11652–11653.

[4] Gambut, L.; Chauvet, J.-P.; Garcia, C.; Berge, B.; Renault, A.; Rivière, S.; Meunier, J.; Collet, A. Ellipsometry, Brewster Angle Microscopy, and Thermodynamic Studies of Monomolecular Films of Cryptophanes at the Air-Water Interface. *Langmuir* **1996**, *12*, 5407–5412.

[5] Kirchhoff, P. D.; Bass, M. B.; Hanks, B. A.; Briggs, J. M.; Collet, A.; McCammon, J. A. Structural Fluctuations of a Cryptophane Host: A Molecular Dynamics Simulation. *J. Am. Chem. Soc.* **1996**, *118*, 3237–3246.

[6] Kirchhoff, P. D.; Dutasta, J.-P.; Collet, A.; McCammon, J. A. Dynamic and Rotational Analysis of Cryptophane Host-Guest Systems: Challenges of Describing Molecular Recognition. *J. Am. Chem. Soc.* **1999**, *121*, 381–390.

[7] Brotin, T.; Lesage, A.; Emsley, L.; Collet, A. 129Xe NMR Spectroscopy of Deuterium-Labeled Cryptophane-A Xenon Complexes: Investigation of Host-Guest Complexation Dynamics. *J. Am. Chem. Soc.* **2000**, *122*, 1171–1174.

[8] Brotin, T.; Roy, V.; Dutasta, J.-P. Improved Synthesis of Functional CTVs and Cryptophanes Using $Sc(OTf)_3$ as Catalyst. *J. Org. Chem.* **2005**, *70*, 6187–6195.

[9] Huber, G.; Brotin, T.; Dubois, L.; Desvaux, H.; Dutasta, J.-P.; Berthault, P. Water Soluble Cryptophanes Showing Unprecedented Affinity for Xenon: Candidates as NMR-Based Biosensors. *J. Am. Chem. Soc.* **2006**, *128*, 6239–6246.

[10] Huber, G.; Beguin, L.; Desvaux, H.; Brotin, T.; Fogarty, H. A.; Dutasta, J.-P.; Berthault, P. Cryptophane-Xenon Complexes in Organic Solvents Observed through NMR Spectroscopy. *J. Phys. Chem. A* **2008**, *112*, 11363–11372.

[11] Bouchet, A.; Brotin, T.; Cavagnat, D.; Buffeteau, T. Induced Chiroptical Changes of a Water-Soluble Cryptophane by Encapsulation of Guest Molecules and Counterion Effects. *Chem. Eur. J.* **2010**, *16*, 4507–4518.

[12] Taratula, O.; Hill, P. A.; Khan, N. S.; Carroll, P. J.; Dmochowski, I. J. Crystallographic observation of 'induced fit' in a cryptophane host–guest model system. *Nat. Commun.* **2010**, *1*, 1–7.

[13] Bouchet, A.; Brotin, T.; Linares, M.; Ågren, H.; Cavagnat, D.; Buffeteau, T. Enantioselective Complexation of Chiral Propylene Oxide by an Enantiopure Water-Soluble Cryptophane. *J. Org. Chem.* **2011**, *76*, 4178–4181.

[14] Bouchet, A.; Brotin, T.; Linares, M.; Cavagnat, D.; Buffeteau, T. Influence of the Chemical Structure of Water-Soluble Cryptophanes on Their Overall Chiroptical and Binding Properties. *J. Org. Chem.* **2011**, *76*, 7816–7825.

[15] Brotin, T.; Montserret, R.; Bouchet, A.; Cavagnat, D.; Linares, M.; Buffeteau, T. High Affinity of Water-Soluble Cryptophanes for Cesium Cations. *J. Org. Chem.* **2012**, *77*, 1198–1201.

[16] Brotin, T.; Cavagnat, D.; Berthault, P.; Montserret, R.; Buffeteau, T. Water-Soluble Molecular Capsule for the Complexation of Cesium and Thallium Cations. *J. Phys. Chem. B* **2012**, *116*, 10905–10914.

[17] Brotin, T.; Goncalves, S.; Berthault, P.; Cavagnat, D.; Buffeteau, T. Influence of the Cavity Size of Water-Soluble Cryptophanes on Their Binding Properties for Cesium and Thallium Cations. *J. Phys. Chem. B* **2013**, *117*, 12593–12601.

[18] Brotin, T.; Berthault, P.; Pitrat, D.; Mulatier, J.-C. Selective Capture of Thallium and Cesium by a Cryptophane Soluble at Neutral pH. *J. Org. Chem.* **2020**, *85*, 9622–9630.

[19] Brotin, T.; Berthault, P.; Chighine, K.; Jeanneau, E. Impact of the Syn/Anti Relative Configuration of Cryptophane-222 on the Binding Affinity of Cesium and Thallium. *ACS Omega* **2022**, *7*, 48361–48371.

[20] Schröder, L.; Lowery, T. J.; Hilty, C.; Wemmer, D. E.; Pines, A. Molecular Imaging Using a Targeted Magnetic Resonance Hyperpolarized Biosensor. *Science* **2006**, *314*, 446–449.

[21] Brotin, T.; Dutasta, J.-P. Cryptophanes and Their Complexes-Present and Future. *Chem. Rev.* **2009**, *109*, 88–130.

[22] Brotin, T.; Martinez, A.; Dutasta, J.-P. In *Calixarenes and Beyond*; Neri, P., Sessler, J. L., Wang, M.-X., Eds.; Springer International Publishing: Cham, 2016; pp 525–557.

[23] Mari, E.; Berthault, P. 129Xe NMR-based sensors: biological applications and recent methods. *Analyst* **2017**, *142*, 3298–3308.

[24] Buffeteau, T.; Pitrat, D.; Daugey, N.; Calin, N.; Jean, M.; Vanthuyne, N.; Ducasse, L.; Wien, F.; Brotin, T. Chiroptical properties of cryptophane-111. *Phys. Chem. Chem. Phys.* **2017**, *19*, 18303–18310.

[25] Barron, L. D.; Buckingham, A. D. Rayleigh and Raman scattering from optically active molecules. *Mol. Phys.* **1971**, *20*, 1111–1119.

[26] Barron, L. D.; Bogaard, M. P.; Buckingham, A. D. Raman scattering of circularly polarized light by optically active molecules. *J. Am. Chem. Soc.* **1973**, *95*, 603–605.

[27] Barron, L. D.; Bogaard, M. P.; Buckingham, A. D. Differential Raman Scattering of Right and Left Circularly Polarized Light by Asymmetric Molecules. *Nature* **1973**, *241*, 113–114.

[28] Barron, L. D.; Buckingham, A. D. Raman circular intensity differential observations on some monoterpenes. *J. Chem. Soc., Chem. Commun.* **1973**, 152–153.

[29] Hug, W.; Kint, S.; Bailey, G. F.; Scherer, J. R. Raman circular intensity differential spectroscopy. Spectra of (-)-α-pinene and (+)-α-phenylethylamine. *J. Am. Chem. Soc.* **1975**, *97*, 5589–5590.

[30] Hug, W.; Hangartner, G. A novel high-throughput Raman spectrometer for polarization difference measurements. *J. Raman Spectrosc.* **1999**, *30*, 841–852.

[31] Hug, W. Virtual Enantiomers as the Solution of Optical Activity's Deterministic Offset Problem. *Applied Spectroscopy* **2003**, *57*, 1–13.

[32] Polavarapu, P. L. Ab initio vibrational Raman and Raman optical activity spectra. *J. Phys. Chem.* **1990**, *94*, 8106–8112.

[33] Bose, P. K.; Polavarapu, P. L.; Barron, L. D.; Hecht, L. Ab initio and experimental Raman optical activity in (+)-(R)-methyloxirane. *J. Phys. Chem.* **1990**, *94*, 1734–1740.

[34] Ditchfield, R.; Miller, D. P. Theoretical carbon-13 nuclear magnetic resonance chemical shifts in CH5+ and C2H5+. *J. Am. Chem. Soc.* **1971**, *93*, 5287–5288.

[35] London, F. Théorie quantique des courants interatomiques dans les combinaisons aromatiques. *J. Phys. Radium* **1937**, *8*, 397–409.

[36] Helgaker, T.; Ruud, K.; Bak, K. L.; Jørgensen, P.; Olsen, J. Vibrational Raman optical activity calculations using London atomic orbitals. *Faraday Discuss.* **1994**, *99*, 165–180.

[37] Ruud, K.; Helgaker, T.; Bouř, P. Gauge-Origin Independent Density-Functional Theory Calculations of Vibrational Raman Optical Activity. *J. Phys. Chem. A* **2002**, *106*, 7448–7455.

[38] Liégeois, V.; Ruud, K.; Champagne, B. An analytical derivative procedure for the calculation of vibrational Raman optical activity spectra. *J. Chem. Phys.* **2007**, *127*, 204105.

[39] Quinet, O.; Champagne, B. Time-dependent Hartree–Fock schemes for analytical evaluation of the Raman intensities. *J. Chem. Phys.* **2001**, *115*, 6293–6299.

[40] Quinet, O.; Liégeois, V.; Champagne, B. TDHF Evaluation of the Dipole–Quadrupole Polarizability and Its Geometrical Derivatives. *J. Chem. Theory Comput.* **2005**, *1*, 444–452.

[41] Cheeseman, J. R.; Frisch, M. J. Basis Set Dependence of Vibrational Raman and Raman Optical Activity Intensities. *J. Chem. Theory Comput.* **2011**, *7*, 3323–3334.

[42] Luber, S.; Reiher, M. Raman optical activity spectra of chiral transition metal complexes. *Chem. Phys.* **2008**, *346*, 212–223.

[43] Thorvaldsen, A. J.; Ruud, K.; Kristensen, K.; Jørgensen, P.; Coriani, S. A density matrix-based quasienergy formulation of the Kohn–Sham density functional response theory using perturbation- and time-dependent basis sets. *J. Chem. Phys.* **2008**, *129*, 214108.

[44] Ruud, K.; Thorvaldsen, A. J. Theoretical approaches to the calculation of Raman optical activity spectra. *Chirality* **2009**, *21*, E54–E67.

[45] Barone, V.; Alessandrini, S.; Biczysko, M.; Cheeseman, J. R.; Clary, D. C.; McCoy, A. B.; DiRisio, R. J.; Neese, F.; Melosso, M.; Puzzarini, C. Computational molecular spectroscopy. *Nat. Rev. Methods Primers* **2021**, *1*, 1–27.

[46] Nafie, L. A. Vibrational optical activity: From discovery and development to future challenges. *Chirality* **2020**, *32*, 667–692.

[47] Fogarty, H. A.; Berthault, P.; Brotin, T.; Huber, G.; Desvaux, H.; Dutasta, J.-P. A Cryptophane Core Optimized for Xenon Encapsulation. *J. Am. Chem. Soc.* **2007**, *129*, 10332–10333.

[48] Daugey, N.; Brotin, T.; Vanthuyne, N.; Cavagnat, D.; Buffeteau, T. Raman Optical Activity of Enantiopure Cryptophanes. *J. Phys. Chem. B* **2014**, *118*, 5211–5217.

[49] Brotin, T.; Daugey, N.; Vanthuyne, N.; Jeanneau, E.; Ducasse, L.; Buffeteau, T. Chiroptical Properties of Cryptophane-223 and -233 Investigated by ECD, VCD, and ROA Spectroscopy. *J. Phys. Chem. B* **2015**, *119*, 8631–8639.

[50] Pitrat, D.; Daugey, N.; Jean, M.; Vanthuyne, N.; Wien, F.; Ducasse, L.; Calin, N.; Buffeteau, T.; Brotin, T. Unusual Chiroptical Properties of the Cryptophane-222 Skeleton. *J. Phys. Chem. B* **2016**, *120*, 12650–12659.

[51] Baydoun, O.; Buffeteau, T.; Daugey, N.; Jean, M.; Vanthuyne, N.; Chapellet, L.-L.; De Rycke, N.; Brotin, T. Chiroptical study of cryptophanes subjected to self-encapsulation. *Chirality* **2019**, *31*, 481–491.

[52] Doll, M.; Berthault, P.; Léonce, E.; Boutin, C.; Buffeteau, T.; Daugey, N.; Vanthuyne, N.; Jean, M.; Brotin, T.; De Rycke, N. Are the Physical Properties of Xe@Cryptophane Complexes Easily Predictable? The Case of syn- and anti-Tris-aza-Cryptophanes. *J. Org. Chem.* **2021**, *86*, 7648–7658.

[53] Grimme, S. Exploration of Chemical Compound, Conformer, and Reaction Space with Meta-Dynamics Simulations Based on Tight-Binding Quantum Chemical Calculations. *J. Chem. Theory Comput.* **2019**, *15*, 2847–2862.

[54] Pracht, P.; Bohle, F.; Grimme, S. Automated exploration of the low-energy chemical space with fast quantum chemical methods. *Phys. Chem. Chem. Phys.* **2020**, *22*, 7169–7192.

[55] Morgante, P.; Ludowieg, H. D.; Autschbach, J. Comparative Study of Vibrational Raman Optical Activity with Different Time-Dependent Density Functional Approximations: The VROA36 Database. *J. Phys. Chem. A* **2022**, *126*, 2909–2927.

[56] Eikås, K. D. R.; Beerepoot, M. T. P.; Ruud, K. A Computational Protocol for Vibrational Circular Dichroism Spectra of Cyclic Oligopeptides. *J. Phys. Chem. A* **2022**, *126*, 5458–5471.

[57] Eikås, K. D. R.; Krupová, M.; Kristoffersen, T.; Beerepoot, M. T. P.; Ruud, K. Can the absolute configuration of cyclic peptides be determined with vibrational circular dichroism? *Phys. Chem. Chem. Phys.* **2023**, *25*, 14520–14529.

[58] Frisch, M. J. et al. Gaussian 16 Revision A.03. 2016; Gaussian Inc. Wallingford CT.

[59] Liégeois, V. DrawMol, DrawProfile, DrawSpectrum, and DrawVib. UNamur, www.unamur.be/sciences/chimie, 2022.

[60] Bannwarth, C.; Caldeweyher, E.; Ehlert, S.; Hansen, A.; Pracht, P.; Seibert, J.; Spicher, S.; Grimme, S. Extended tight-binding quantum chemistry methods. *WIREs Comput. Mol. Sci.* **2021**, *11*, e1493.

[61] Bannwarth, C.; Ehlert, S.; Grimme, S. GFN2-xTB—An Accurate and Broadly Parametrized Self-Consistent Tight-Binding Quantum Chemical Method with Multipole Electrostatics and Density-Dependent Dispersion Contributions. *J. Chem. Theo. Comput.* **2019**, *15*, 1652–1671.

[62] Caldeweyher, E.; Ehlert, S.; Hansen, A.; Neugebauer, H.; Spicher, S.; Bannwarth, C.; Grimme, S. A generally applicable atomic-charge dependent London dispersion correction. *J. Chem. Phys.* **2019**, *150*, 154122.

[63] Hibbert, D. B. Generation and display of chemical structures by genetic algorithms. *Chemometrics Intell. Lab. Sys.* **1993**, *20*, 35–43.

[64] Leardi, R. Genetic algorithms in chemometrics and chemistry: a review. *J. Chemometrics* **2001**, *15*, 559–569.

[65] Vainio, M. J.; Johnson, M. S. Generating Conformer Ensembles Using a Multiobjective Genetic Algorithm. *J. Chem. Inf. Model.* **2007**, *47*, 2462–2474.

[66] Scott, A. P.; Radom, L. Harmonic vibrational frequencies: An evaluation of Hartree-Fock, Møller-Plesset, quadratic configuration interaction, density functional theory, and semiempirical scale factors. *J. Phys. Chem.* **1996**, *100*, 16502–16513.

[67] Reiher, M.; Liégeois, V.; Ruud, K. Basis Set and Density Functional Dependence of Vibrational Raman Optical Activity Calculations. *J. Phys. Chem. A* **2005**, *109*, 7567–7574.

[68] Lee, C.; Yang, W.; Parr, R. G. Development of the Colle-Salvetti correlation-energy formula into a functional of the electron density. *Phys. Rev. B* **1988**, *37*, 785–789.

[69] Becke, A. D. Density-functional thermochemistry. III. The role of exact exchange. *J. Chem. Phys.* **1993**, *98*, 5648–5652.

[70] Zuber, G.; Hug, W. Rarefied Basis Sets for the Calculation of Optical Tensors. 1. The Importance of Gradients on Hydrogen Atoms for the Raman Scattering Tensor. *J. Phys. Chem. A* **2004**, *108*, 2108–2118.

[71] Long, D. A. *The Raman Effect: A Unified Treatment of the Theory of Raman Scattering by Molecules*; Wiley, 2001.

[72] Hug, W. Visualizing Raman and Raman optical activity generation in polyatomic molecules. *Chem. Phys.* **2001**, *264*, 53–69.

[73] Barron, L. D. *Molecular Light Scattering and Optical Activity*, 2nd ed.; Cambridge University Press, 2004.

[74] Hug, W. *Handbook of vibrational spectroscopy*; John Wiley & Sons, Ltd, 2006; pp 745–758.

[75] Peterson, K. A.; Figgen, D.; Goll, E.; Stoll, H.; Dolg, M. Systematically convergent basis sets with relativistic pseudopotentials. II. Small-core pseudopotentials and correlation consistent basis sets for the post-d group 16–18 elements. *J. Chem. Phys.* **2003**, *119*, 11113–11123.

[76] LaJohn, L. A.; Christiansen, P. A.; Ross, R. B.; Atashroo, T.; Ermler, W. C. Ab initio relativistic effective potentials with spin–orbit operators. III. Rb through Xe. *J. Chem. Phys.* **1987**, *87*, 2812–2824.

[77] Wadt, W. R.; Hay, P. J. Ab initio effective core potentials for molecular calculations. Potentials for main group elements Na to Bi. *J. Chem. Phys.* **1985**, *82*, 284–298.

[78] Stevens, W. J.; Krauss, M.; Basch, H.; Jasien, P. G. Relativistic compact effective potentials and efficient, shared-exponent basis sets for the third-, fourth-, and fifth-row atoms. *Can. J. Chem.* **1992**, *70*, 612–630.

[79] Nicklass, A.; Dolg, M.; Stoll, H.; Preuss, H. Ab initio energy-adjusted pseudopotentials for the noble gases Ne through Xe: Calculation of atomic dipole and quadrupole polarizabilities. *J. Chem. Phys.* **1995**, *102*, 8942–8952.

[80] Reichman, S.; Schreiner, F. Gas-Phase Structure of XeF_2. *J. Chem. Phys.* **1969**, *51*, 2355–2358.

[81] Levy, H. A.; Agron, P. A. The Crystal and Molecular Structure of Xenon Difluoride by Neutron Diffraction. *J. Am. Chem. Soc.* **1963**, *85*, 241–242.

[82] Burns, J. H.; Agron, P. A.; Levy, H. A. Xenon Tetrafluoride Molecule and Its Thermal Motion: A Neutron Diffraction Study. *Science* **1963**, *139*, 1208–1209.

[83] Burbank, R. D.; Jones, G. R. Structure of the cubic phase of xenon hexafluoride at 193.deg.K. *J. Am. Chem. Soc.* **1974**, *96*, 43–48.

[84] Malm, J. G.; Selig, H.; Jortner, J.; Rice, S. A. The Chemistry Of Xenon. *Chem. Rev.* **1965**, *65*, 199–236.

[85] Tomasi, J.; Mennucci, B.; Cammi, R. Quantum mechanical continuum solvation models. *Chem. Rev.* **2005**, *105*, 2999–3093.

[86] Marenich, A. V.; Olson, R. M.; Kelly, C. P.; Cramer, C. J.; Truhlar, D. G. Self-Consistent Reaction Field Model for Aqueous and Nonaqueous Solutions Based on Accurate Polarized Partial Charges. *J. Chem. Theory Comput.* **2007**, *3*, 2011–2033.

[87] Marenich, A. V.; Cramer, C. J.; Truhlar, D. G. Universal Solvation Model Based on Solute Electron Density and on a Continuum Model of the Solvent Defined by the Bulk Dielectric Constant and Atomic Surface Tensions. *J. Phys. Chem. B* **2009**, *113*, 6378–6396.

[88] Nilsson Lill, S. O. Evaluation of dispersion-corrected density functional theory (B3LYP-DCP) for compounds of biochemical interest. *J. Mol. Graph. Model.* **2010**, *29*, 178–187.

[89] Michal, P.; Čelechovský, R.; Dudka, M.; Kapitán, J.; Vůjtek, M.; Berešová, M.; Šebestík, J.; Thangavel, K.; Bouř, P. Vibrational Optical Activity of Intermolecular, Overtone, and Combination Bands: 2-Chloropropionitrile and α-Pinene. *J. Phys. Chem. B* **2019**, *123*, 2147–2156.

[90] Hopmann, K. H.; Šebestík, J.; Novotná, J.; Stensen, W.; Urbanová, M.; Svenson, J.; Svendsen, J. S.; Bouř, P.; Ruud, K. Determining the Absolute Configuration of Two Marine Compounds Using Vibrational Chiroptical Spectroscopy. *J. Org. Chem.* **2012**, *77*, 858–869.